TÉCNICO LISBOA

Design loading optimization of a horizontal axis turbine with lifting line and panel methods

Emanuele Quarona

Thesis to obtain the Master of Science Degree in

Energy Engineering and Management

Supervisors: Prof. José Alberto Caiado Falcão de Campos

Dr. João Manuel Ribeiro da Costa Baltazar

Examination Committee

Chairperson: Prof. Jorge de Saldanha Gonçalves Matos

Supervisor: Prof. José Alberto Caiado Falcão de Campos

Member of the Committee: Prof. Luís Manuel de Carvalho Gato

October 2019

Acknowledgments

I would first like to thank my two thesis supervisors, Professors José Falcão de Campos and João Baltazar for giving me the opportunity to work in a field that I really like. The assistance and help provided by them was highly appreciated, as well as the availability shown.

Afterwards, I must express my very profound gratitude to my family for providing me unfailing support and continuous encouragement throughout my years of studies. This accomplishment would not have been possible without them and their sacrifices.

Finally, I would like to thank all my friends: the ones back home, the ones I met during this Master Programme and the ones spread all over. Thanks for making my life fun and for always being so close no matter the distance.

Abstract

The objective of this work is to improve the wake alignment procedure implemented in an already existing lifting line code for optimal loading design of a wind turbine. For that purpose, a combination of a lifting line code and a panel method code is proposed. In particular, through a cycle (repeated twice), the lifting line code provides the design of the wind turbine blade which is analysed by the panel method code, giving as output the wake geometry that will be used in the next cycle to update the design of the blade with the lifting line code.

The lifting line theory and the panel method (also known as boundary element method) are presented, together with the corresponding numerical models.

The computational procedure is explained step by step and the convergence analysis performed shows how the discretization and iteration errors affect the results obtained.

With the assumption of inviscid flow, the design cycle is carried out delivering the optimum circulation distribution and from there the blade chord and the pitch are obtained. The wake geometry presents the expected characteristics, folding downstream, even close to the rotor plane.

Next the viscous effects on lift and drag are included in the design cycle .The results are not that different from the inviscid ones: the wake geometry is similar, the only remarkable difference lies on the chord distribution where the values are higher because of the lower lift coefficient compared to the one chosen for the inviscid case.

Overall, the results are successful and the comparison with the previous cases show that the wake alignment procedure has been improved.

Keywords: Lifting line theory; Panel method; Wind turbine; Wake alignment.

Resumo

O objetivo deste trabalho compreende o melhoramento de um método de alinhamento da esteira, implementado num código de linha sustentadora existente e desenvolvido para o projeto da carga ótima em turbinas eólicas. Nesse sentido, propõe-se uma combinação entre o código da linha sustentadora e um código de método de painel. Em particular, através de um ciclo iterativo (repetido duas vezes), o código de linha sustentadora proporciona o projeto das pás da turbina eólica, que depois são analisadas pelo código de método de painel, onde se obtém a geometria da esteira das pás que serão utilizadas no ciclo seguinte para um novo projeto das pás da turbina eólica com o código da linha sustentadora.

Apresentam-se os modelos da linha sustentadora e do método de painel (também conhecido por método de elementos de fronteira), juntamente com os correspondentes modelos numéricos.

O procedimento computacional é explicado em detalhe e um estudo de convergência é apresentado para mostrar a influência dos erros de discretização e iterativos nos resultados.

Começando pela hipótese de escoamento invíscido, o ciclo de projeto é executado para a obtenção da distribuição de circulação ótima, e das distribuições de corda e passo da pá. A geometria da esteira das pás apresenta as características esperadas, desenvolvendo-se para jusante.

De seguida, os efeitos viscosos na sustentação e resistência dos perfis são incluídos no ciclo de projeto. Resultados semelhantes são obtidos em comparação com o caso invíscido: as geometrias da esteira das pás são semelhantes, e a única diferença significativa verifica-se na distribuição de corda, que apresenta valores mais altos devido ao inferior coeficiente de sustentação em comparação com o escolhido para o projeto invíscido.
Globalmente, os resultados apresentados são satisfatórios e a comparação com os casos anteriores mostra que o método de alinhamento da esteira foi aperfeiçoado.

Palavras-chave: Teoria da linha sustentadora; Método dos painéis; Turbina eólica; Alinhamento de esteira.

Contents

List of Tables

List of Figures

Nomenclature

Greek symbols

α	Angle of attack
β	Undisturbed aerodynamic pitch angle
β_i	Induced aerodynamic pitch angle
Γ	Circulation
γ	Intensity of the trailing vortices
ε	Drag to lift ratio
ε_N	Numerical tolerance for the aerodynamic pitch angle
θ_K	Angular position of the k^{th} lifting line
k_N	Under-relaxation factor for the aerodynamic pitch angle
λ	Tip speed ratio
ν	Kinematic viscosity of the fluid
ρ	Volumetric mass density of the fluid
ψ	Blade pitch angle
ω	Angular velocity of the rotor
μ	Dipole strength
δ	Knonecker delta
σ	Source strength
ϕ	Perturbation potential

Roman symbols

c	Section chord
C_D	Drag coefficient
C_L	Lift coefficient
C_{L_v}	Lift coefficient – viscous case
C_{L_i}	Lift coefficient – inviscid case
C_P	Power coefficient
C_T	Thrust coefficient
C_{T_0}	Imposed thrust coefficient
$C_{a,t_{ij}}$	Axial and tangential influence coefficients matrices
D	Drag force per unit span
$\vec{e}$	Unit vector
H	Auxiliary function used in the Lagrange Multiplier Method

l	Constant; Lagrange multiplier
$\vec{L}$	Lift force by unit span
L_k	Lifting line k
M	Number of segments in which the lifting line is discretized
N	Number of sections in which a trailing vortex is discretized
n_s	Number of wake alignment sections
N_t	Number of equal stream-wise segments per revolution used in the wake discretization
p	Dimensionless wake pitch
Q	Torque
$\vec{R}$	Vector of distance
R	Rotor radius
r_h	Hub radius
$\bar{r}_i$	Radial position of control point i
r_j	Radial position of end point j
s	Stream-wise direction
S_k	Vortex sheet shed from lifting line k
T	Axial force
U , U_e	Velocity of the incoming flow
$\vec{V}$	Total velocity
$\vec{V}_\infty$	Undisturbed velocity
$\vec{v}$	Velocity induced by the entire system of vortices
V , V_t	Magnitude of projections of the total velocity vector on the blade cross section
$\vec{v}_k$	Velocity induced by the k^{th} lifting line and its sheet of trailing vortices
x, r, θ	Cylindrical coordinates in the rotating reference frame
x_{fw}	Axial position of the far wake section
x_{uw}	Axial position of the ultimate section, where the wake is truncated
Z	Number of rotor blades
$\vec{n}$	Unit vector perpendicular to a surface
n_x, n_y, n_z	Cartesian coordinates of a vector perpendicular to a surface
S_W	Wake surface
S_B	Blade surface
S_H	Hub surface
G	Distance between a field point and a point on the boundary
D_{ij}^k , S_{ij}^k	Influence coefficients
W_{iml}^k	Wake influence coefficients
N_{rev}	Number of revolutions

Subscripts

a	Projection on the axial direction
r	Projection on the radial direction
t	Projection on the tangential direction
x	Projection on the direction of x
y	Projection on the direction of y
z	Projection on the direction of z
k	Related to the blade
B	Related to the blade surface
H	Related to the blade surface
W	Related to the wake surface
∞	Related to the undisturbed flow
S	Related to a surface
$t.e.$	Related to the trailing edge points
$l.l$	Related to the lifting line points

Superscripts

$'$	Relative to image vortex
$*$	Non-dimensional quantity
$+$	Related to the right side of a surface
$-$	Related to the left side of a surface

1 Introduction

A horizontal wind turbine is a device that transforms a part of the wind kinetic energy (air in motion) into available mechanical energy that is then converted in electrical energy by a generator. The wind turbines have three main components (Yahyaoui, 2018):

- the tower, that gives support and avoid disturbances near the ground;
- the nacelle, which bring together all the mechanical elements allowing to couple the wind turbine's electric generator;
- the rotor, which is composed by a number of blades that goes from 1 to 3 (Danish concept turbine);

Figure 1: Offshore wind turbine farm. (Sun&Wind Energy, 2017)

In a world where the population is drastically increasing, meeting the demand of energy while keeping the increase of the global temperature below 2°C , as it was decided in the Paris Agreement (UNFCCC, 2018), is an ambitious goal and the renewable technologies can be one of the keys to enable that. (EIA, 2017)

According to the BP Energy Outlook Report (BP, 2018), when looking at the 2040 forecasts, the renewables are the largest source of energy growth: their share of power generation by source is shown in Figure 2 and it is possible to see the vital role that wind energy has and will have in the electricity global scenarios.

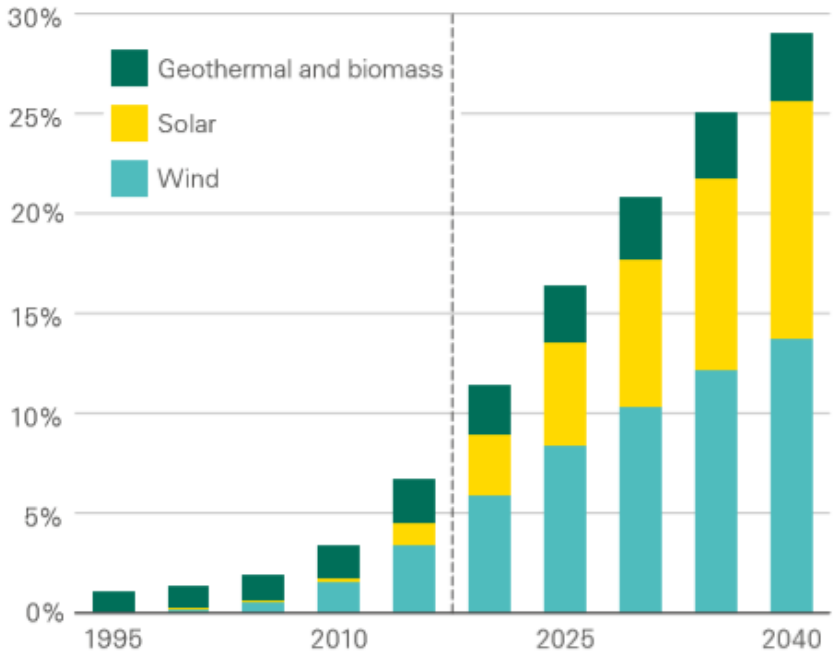

Figure 2: Forecast of the renewable power generation shares in the next decades. (BP, 2018)

Now that the importance of the wind industry worldwide is clear, it is easily understandable why the improvements of the optimization, design and analysis computational codes of the wind turbines are so important for the sustainability, both from the economical and environmental point of view.

This thesis presents a iterative procedure to obtain more accurate optimal loading design of the wind turbine rotor while combining two methods that have been largely used in the propellers industry.

1.1 State of the art

Since the end of the 19th century, the improvements in the aerodynamics and fluid mechanics fields have been remarkable. The formulation of the lifting line theory surely gave fundamental insights for the development of many technologies. It was Frederick W. Lanchester, engineer and then manager of his own car company that in 1907, after years of studying on the flight characteristics, set the basics for the lifting line theory (Lanchester, 1907). The three Helmholtz's vortex theorems were already published at that time, therefore Lanchester knew that the vortex could not vanish at the tip of the wing, that is the reason why he assumed that the vortex was shed from the tip of the wing and would continue in the wake (Lighthill & Berger, 2008).

In 1919, Ludwig Prandtl, working with his students Albert Betz and Max Munk, formulated a more accurate theory stating that the vortex loses strength along the whole wingspan because it is shed as a vortex-sheet from the trailing edge, rather than just at the wing-tips. (Prandtl, 1918)

From this point on many improvements were done to the theory according to the applications of it, in fact the lifting line has been used for the design and analysis of many lifting surfaces like wings, propellers and ultimately horizontal axis wind turbines. (Abbott, 1959)

The lifting line theory, originally introduced for wings, was then applied to propellers (Betz, 1919) (Goldstein, 1929). In particular, Betz set the conditions for the classical optimization with restrictive constraints such as: light load and absence of viscous forces, blades as radial bound vortices of varying circulation from which free helical vortices with constant pitch are shed; afterwards Goldstein solved the potential flow problem obtaining the circulation distribution for a hubless propeller.

Lerbs (1952) extended the work to moderately loaded propellers using the induction factor concept elaborated in Kawada (1933), finding the induced velocities from the system of vortices. In this model the pitch of the vortex helicoidal lines must be found by aligning the trailing vortices with the local fluid velocity at the lifting lines and it is constant along the axial direction but not along the radial one.

Finally Maekawa (1986) adapted the optimization criteria for the wind turbines managing to present a design procedure using the developments done by Betz and Goldstein.

From that time to the beginning of the 2000s, some corrections such as the inclusion of viscous drag by Adkins & Liebeck (1994) were implemented. Chattot (2003) worked on the optimization of horizontal axis turbines with a helical vortex model using Biot-Savart integration for the induced velocities. However, those authors were still considering a rigid helicoidal wake which limits the application of the lifting line theory to moderately loaded rotors, that is the reason why through the last 30 years the alignment of the wake geometry with the local velocity became a crucial matter to consider. Only in this way the computation of induced velocities, axial and power coefficients could have been improved and considered fully reliable.

At the MARETEC/IST extensive work has been done on the design optimization of propellers and wind turbines: Duarte & Falcão de Campos (1997) developed a lifting line code that was later improved by Falcão

de Campos (2007) in his work about optimization of a marine current turbine. Machado (2010) then added the effect of the hub and Caldeira (2014) added the viscous effects. Melo (2016), using the numerical approach by Baltazar, Falcão de Campos, & Bosschers (2012), implemented the analysis code for wind turbines adding a wake alignment scheme and Sousa (2018) succeeded to perform the optimization procedure adjusting the analysis code by Melo and implementing the Lagrange multiplier method instead of the classical one so far used. Many parametric studies were also conducted on this last version of the code, changing the tip speed ratios, the lift to drag coefficient, including the hub or not and a comparison and discussion on the wake geometries obtained was accurately made.

However, the lifting line theory models the surfaces as lines and even the most updated version of the lifting line code suffers from the drawback that the flow in vicinity of the blades is not accurately modelled. Therefore, over the century new computational based theories were developed such as the panel methods (1970s). With this model it is possible to take into account the geometry of the blades and it is possible to obtain a more accurate description of how the fluid behaves along the blade, at the trailing edge and at the wake region. (Erickson, 1990)

At the MARETEC/IST centre integral boundary element method (panel method) codes were also developed for the analysis of horizontal marine current turbines resulting in a better description of the flow around the blades. The panel method was widely used by many authors like Kerwin, Member, Kinnas, & Le (1987) for the design and the hydrodynamic analysis of marine propellers and Baltazar & Falcão de Campos (2011) adapted it to the case of marine current turbines. The in-house IST panel code (PROPAN) provides information on the pressure distribution around the blades and predicts the blade cavitation performance.

The panel method has been largely used in the maritime community. The CNR-INSEAN (National Research Council, Marine Technology Research Institute) proposed a computational methodology for the hydrodynamic analysis of a horizonal axis marine current turbines using a boundary integral equation method for inviscid flow, following the same approach used for marine propellers (Salvatore, Sarichloo, & Calcagni, 2018).

In regards to the application of the panel method to wind turbines there are not many research centers or university worldwide exploring it. However, some works on this topic can be mentioned. In order to understand the extreme loading effects on the rotor to prevent failures, Nelson & Kouh (2017) proposed a viscous-coupled 3D panel method which introduces a novel approach to simulating the severe flow separation so prevalent around wind turbine rotors. The results obtained show very good agreement with the ones coming through RANS method and for this reason the authors state the usefulness of their work, even in future design or analysis procedures. Another work that lead to promising results is the analysis on a NREL turbine (Hogan, 2010): in his thesis, Hogan managed to show that the panel code PROPAN could be suitable to the study of wind turbine rotors too. In fact, the agreement between the numerical and experimental results was good.

As it will be further explained in the next sections, the focus of this thesis is the combination of the lifting line method with the panel method for the optimal loading design of a horizontal axis wind turbine, this

allows to obtain a more accurate wake geometry and therefore improved optimization of the design of the blades.

1.2 Objective of the thesis

The purpose of this thesis is to improve the optimization procedures so far implemented by many authors combining in an iterative way the lifting line optimization code updated by Sousa in 2018 with a panel code able to analyse the blade design of a horizontal axis turbine according to specific wind conditions. In other words, with the lifting line code the optimum circulation distribution is found first and based on that the design of the rotor can be done. Then, the panel code analyses the rotor and provides the wake geometry that is used again in the lifting line code as input, to get a circulation distribution adapted to the actual aligned wake found with the panel code. This cycle is repeated a certain number of times to get the convergence of the design parameters. The effect of the viscous forces in the design is also investigated. This thesis aims to show that the alignment procedure adopted in this way leads to more physically acceptable results compared to the previously alignment methods, especially in terms of aerodynamic pitch.

1.3 Thesis outline

The thesis is divided in chapters as follows:

- The Chapter 2 presents the theory fundamentals of the lifting line theory and the panel method applied to the wind turbine rotor. The induced velocities, the forces and the wake model are presented, as well as the most significant variables to describe the physical phenomena and the performance.
- Chapter 3 is divided in four subchapters. In the numerical model sections, the discretization of the lifting line and the computation of the induced velocities is presented. The inclusion of the hub in the model and the methods of optimization are briefly explained. There is also a description on the discretization done in the panel code, how the integral equation is solved and the Kutta condition which is a pillar of this theory. Then, the computational procedure is explained step by step. Finally, a convergence analysis shows how the discretizations and the computational choices made in the panel code affect the accuracy of the results obtained.
- The results are presented in Chapter 4. The choice of the lift coefficient for the inviscid and viscous situation is motivated, then some approximations and issues faced during the computations are discussed. Then, there are three subchapters with the result for the inviscid flow, the viscous one and a comparison among the two cases. The circulation, the chord, the blade pitch, the aerodynamic pitch and the pressure distribution are discussed.
- Finally, the main outcomes are summarized in the Conclusion chapter, together with some suggestions aiming to improve the current model.

2 Theory

2.1 Introduction to lifting line theory

Lanchester and Prandtl were the first ones that elaborated a mathematical model that predicts the lift distribution over a three-dimensional wing based on its geometry, which will then be called as lifting line theory (Anderson, 2001).

The theory, first developed for wings, was successively adapted to propellers and later to wind and marine turbines. According to it, the bound vortex represents the lifting line and it loses strength along the whole wingspan since it is shed as a vortex-sheet from the trailing edge. (Abbott, 1959)

The theory uses the circulation concept and the Kutta-Joukowski theorem:

$$\vec{L} = -\rho \overrightarrow{V_\infty} \times \vec{\Gamma}, \tag{1}$$

where ρ and $\overrightarrow{V_\infty}$ are respectively the density and the velocity far upstream and $\vec{\Gamma}$ is the strength of the bound vortex representing the lifting line, its magnitude formula is $\Gamma = \oint \vec{V} \cdot \overrightarrow{ds}$ and that represents the circulation defined as the line integral around a closed contour enclosing the airfoil. With this formula the unknown becomes the circulation function instead of the lift force, in fact the span-wise change in lift is equivalent to a span-wise change of circulation. (Anderson, 2001)

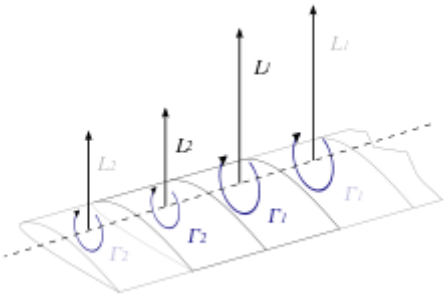

Figure 3: Lift distribution over a wing modeled as circulation distribution. (Gallard, 2014)

As already mentioned in the Introduction, according to Helmholtz's theorems, a vortex filament cannot begin or terminate in the fluid. Any span-wise change in lift can be modelled as the shedding of a vortex filament downstream to the flow, behind the wing.

It is necessary to mention that for three-dimensional lifting bodies, the lift does not correspond to what the two-dimensional theory predicts because the local lift (lift per unit span) is influenced by the lift generated at the neighboring wing sections. In fact, the lift is usually proportional to the pressure difference between the upper and the lower surface of the blade and at the tip of the blade the difference becomes zero and the

secondary flow appears: the fluid tends to move around the tip, going up to the low pressure surface of the blade. The circulation distribution and consequently the lift will depend on the pressure distribution, resulting zero at the tip. A wing modelled as circulation distribution is shown in Figure 3, and the same will be done for the wind turbine blades.

Through this section, the main pillars of the theory and how it models the behaviour of the flow and its effect will be discussed.

2.1.1 Velocity field

Consider the rotor of a horizontal axis wind turbine with radius R and hub radius r_h and Z blades symmetrically placed around the hub. Assume the rotor rotating with an angular velocity ω in a uniform flow velocity field U, aligned with the rotation axis. It is possible to define a cartesian coordinate system (x, y, z) and a cylindrical coordinate system (x, r, θ) in a reference frame rotating with the turbine rotor. The relative velocity field is given by $\overrightarrow{V_\infty} = \vec{U} - \overrightarrow{\omega} \times \vec{r}$, as shown in Figure 4.

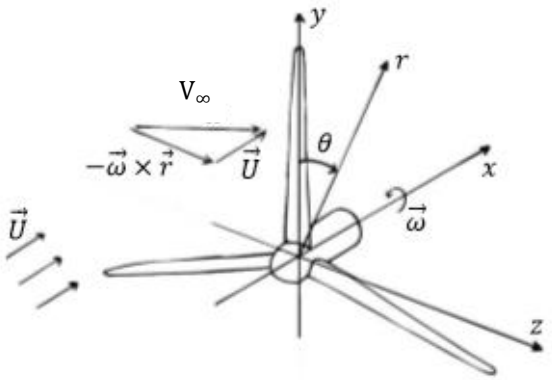

Figure 4: Adopted coordinate system and inflow velocity field, $Z = 3$. (Melo, 2016)

In the lifting line model, every blade is represented by a radial bound vortex, expanding from the root of the blade to the tip. The circulation along the lifting line is not constant and can be represented by a vector:

$$\vec{\Gamma}(r) = -\Gamma(r)\vec{e}_r, \tag{2}$$

where $\vec{e}_r$ is the radial unit vector. Due to the variation of circulation along the blade, trailing vortices are shed from each lifting line, generating a vortex sheet. The intensity of those vortices can be found from the Helmoltz's theory:

$$\vec{\gamma} = \frac{d\Gamma(r)}{dr}\vec{e}_s, \tag{3}$$

where $\vec{e}_s$ is a unit vector tangent to the vortex sheet and aligned with the vortex filaments. In Figure 5 it is possible to see the vortex system for one of the blades.

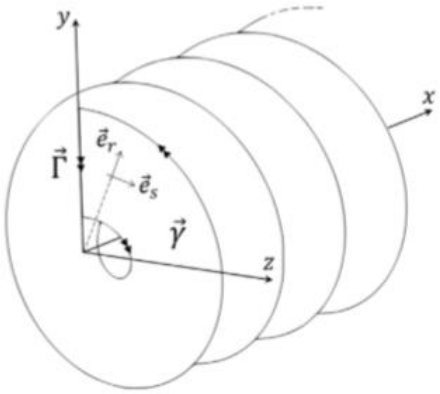

Figure 5: Lifting line (one blade) and corresponding vortex sheet. (Melo, 2016)

It is important to remark that in the force-free vortex wake, the vortex filaments must be aligned with the local velocity field giving the product $\vec{\gamma} \times \vec{V} = 0$.

The velocity field without considering the influence of the vortices is:

$$\vec{V}(x, r, \theta) = (U, 0, \omega r). \tag{4}$$

Considering the effect of the bound and the trailing vortices, the velocity induced by the lifting line k and its sheet of trailing vortices can be computed in any point in space by the Biot Savart law:

$$\vec{v}_k(x, y, z) = \frac{1}{4\pi}\int_{L_k} \frac{\vec{\Gamma}\times\vec{R}}{R^3} dl + \frac{1}{4\pi}\int_{S_k} \frac{\vec{\gamma}\times\vec{R}}{R^3} dS, \tag{5}$$

where $\vec{R}$ is the vector going from the integration point to the point (x, y, z) where the computation of the induced velocities is being done. When the computation of the induced velocities is done on one of the lifting lines, the first integral can be omitted, because of the symmetry of the rotor, so only the trailing vortices have to be considered.

The total induced velocities are obtained by the sum of the Z blades contributions:

$$\vec{v}(x, y, z) = \sum_{k=1}^{Z} \vec{v}_k(x, y, z). \tag{6}$$

At this point, summing up the total induced velocities and the undisturbed velocity field component it is possible to get the velocity field in cylindrical coordinates:

$$\vec{V}(x, r, \theta) = (U - v_a, v_r, \omega r + v_t), \tag{7}$$

where the induced velocities components are:

$$v_a = -v_x, \tag{8}$$

$$v_r = v_y \cos\theta + v_z \sin\theta, \tag{9}$$

$$v_t = -v_y \sin\theta + v_z \cos\theta, \tag{10}$$

where θ is the angular coordinate is the plan $y - z$ of Figure 5.

2.1.2 Angles, forces and power coefficients

A velocity triangle can now be drawn as in Figure 6 and some of the illustrated angles can be explained:

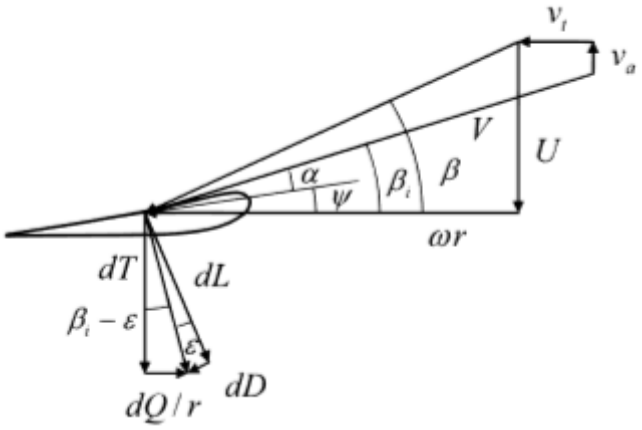

Figure 6: Schematic representation of the velocity and force triangles at a blade section. (Melo, 2016)

- β is the undisturbed aerodynamic pitch angle, which is the angle between the undisturbed velocity and the tangential direction. The formula is:

$$\tan\beta = \frac{U}{\omega r} = \frac{1}{\lambda r^*}, \tag{11}$$

where $r^* = \frac{r}{R}$ and λ is the tip speed ratio, defined as:

$$\lambda = \frac{\omega R}{U}. \tag{12}$$

- β_i is the induced aerodynamic pitch angle, which includes the effect of the axial and tangential induced velocities:

$$\tan\beta_i = \frac{U - v_a}{\omega r + v_t} = \frac{1 - v_a^*}{\lambda r^* + v_t^*}, \tag{13}$$

where the induced velocities are made dimensionless: $v_{a,t}^* = \frac{v_{a,t}}{U}$.

- α is the angle of attach, angle between the section chord line and the velocity projected on the blade cross section.

- ψ is the blade pitch angle, which is geometrical angle between the blade chord line and the tangential direction, which is related with β_i and α by:

$$\psi = \beta_i - \alpha. \tag{14}$$

The total velocity V can be expressed in a dimensionless way with the formula:

$$V^* = \frac{V}{U} = \sqrt{(1 - v_a^*)^2 + (\lambda r^* + v_t^*)}. \tag{15}$$

Recalling the Kutta-Joukowsky theorem it is now possible to proceed explaining the forces involved between the fluid and the blades. In fact, from the formula $\vec{L} = -\rho\vec{V} \times \vec{\Gamma}$ it is clear that the lift force is the component of the resulting force perpendicular to the incoming disturbed flow.

The radial components of the induced velocities do not contribute to the lifting force, because the circulation vector $\vec{\Gamma}$ is aligned with the lifting line making the cross product $\vec{v}_r \times \vec{\Gamma}$ equal to zero.

The lifting force per unit span is given by:

$$L = \rho V \Gamma, \tag{16}$$

where V is the velocity projected on the blade cross section, calculated previously, not including the component v_r for the reason aforementioned.

Going back to Figure 6 it is now possible to mention the various components of the resulting force acting of the blade that appear:

L - Lift (per unit span). It is the projection of the resulting force in the direction perpendicular to $\vec{V}$;

D - Drag (per unit span). It is the projection of the resulting force in the same direction as $\vec{V}$ due to viscous effects;

T - Thrust. Projection of the resulting force in the axial direction;

Q/r - Circumferential force. Force that contributes to the torque in the tangential direction.

The most important dimensionless coefficients are:

$$C_L = \frac{L}{\frac{1}{2}\rho V^2 c} = \frac{2\Gamma}{Vc} = \frac{2\Gamma^*}{V^* c^*}, \tag{17}$$

$$C_D = \frac{D}{\frac{1}{2}\rho V^2 c}, \tag{18}$$

$$C_T = \frac{T}{\frac{1}{2}\rho U^2 \pi R^2}, \tag{19}$$

$$C_P = \frac{P}{\frac{1}{2}\rho U^3 \pi R^2}. \tag{20}$$

When the star * appears, it means that those specific variables are non-dimensional, that is the case of the circulation Γ , the chord c, and the total velocity V.

The C_L and C_D data are usually given for a specific foil as function of the angle of attack and the Reynolds number Re defined as: $Re = \frac{Vc}{\nu}$, where ν is the kinematic viscosity of the fluid. They are usually obtained experimentally. The drag to lift coefficient $D/L = C_D/C_L$ is a very important parameter and it is usually represented with the letter ε.

Integrating along the span the infinitesimal thrust, considering the Z blades it is possible to get the thrust coefficient as:

$$C_T = \frac{2Z}{\pi} \int_{r_h^*}^{1} (\lambda r^* + v_t^*)\, \Gamma^* (1 + \varepsilon \tan\beta_i)\, dr^*. \tag{21}$$

The same can be done for the power coefficient:

$$C_P = \frac{2Z\lambda}{\pi} \int_{r_h^*}^{1} (1 - v_a^*)\, \Gamma^* \left(1 - \frac{\varepsilon}{\tan\beta_i}\right) r^* dr^*. \tag{22}$$

2.2 Introduction to the panel method

As already mentioned, in the last decades the panel method, widely used for aircrafts and propellers, has been used for turbines too. This method allows a better understanding of the behaviour of the fluid around the blades. The hub, the blades and the wakes are discretized in panels and solving the potential flow equation the velocity in each panel is obtained and the pressure from the Bernoulli equation too. The main assumptions that lies under the method are inviscid, incompressible and irrotational flow.

2.2.1 Potential flow method

In Figure 7 a rotor subjected to an inflow is illustrated. This inflow is assumed to be steady in the cartesian inertial frame (x_0, y_0, z_0) and the inflow velocity to the turbine is $U_e = (x_0, y_0, z_0)$.

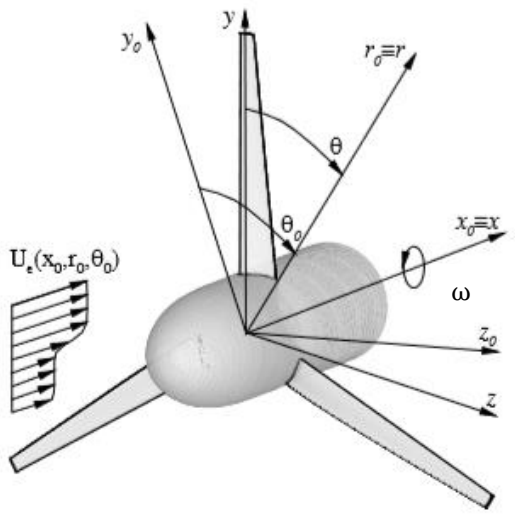

Figure 7: Rotor inflow and coordinate systems. (Baltazar & Falcão de Campos, 2009)

In the reference frame rotating with the turbine, the undisturbed inflow velocity is given by:

$$\overrightarrow{V_\infty}(x, r, \theta, t) = \overrightarrow{U_e}(x, r, \theta - \omega t) - \vec{\omega} \times \vec{x}, \tag{23}$$

where $\vec{x} = (x, y, z)$. In the reference frame rotating with the turbine, and under the assumption of irrotational flow the velocity field is described by a perturbation potential $\phi(x, y, z, t)$:

$$\vec{V}(x, y, z, t) = \vec{V}_\infty(x, y, z, t) + \nabla\phi(x, y, z, t). \tag{24}$$

The perturbation potential satisfies the Laplace equation:

$$\nabla^2\phi(x, y, z, t)=0. \tag{25}$$

The boundary of the domain consists of the turbine blade surfaces S_B and the hub surface S_H. The perturbation potential must satisfy the following boundary conditions:

$$\nabla\phi \to 0, \text{ if } |\vec{x}| \to \infty \text{ and } x \neq +\infty, \tag{26}$$

at infinity, and a Neumann boundary condition:

$$\frac{\partial\phi}{\partial n} \equiv \vec{n} \cdot \nabla\phi = -\vec{n} \cdot \vec{V}_\infty \text{ on } S_B \text{ and } S_H, \tag{27}$$

where $\partial/\partial n$ denotes differentiation along the normal and $\vec{n}$ is the unit vector normal to the surface directed outward from the body. The boundary conditions on the wake surfaces S_W are the tangency of the fluid velocity on each side of the sheet:

$$\vec{V}_w \cdot \vec{n} = \vec{V}^+ \cdot \vec{n} = \vec{V}^- \cdot \vec{n} \text{ on } S_W, \tag{28}$$

and the continuity of the pressure across the vortex wake:

$$p^+ = p^- \text{ on } S_W, \tag{29}$$

where $\vec{V}$ is the fluid velocity, $\vec{V}_w$ the velocity of the vortex sheet surface S_W, p is the pressure and the indices + and − denote the two sides of the vortex sheet, arbitrarily chosen on the upper side and lower side of the blade at the trailing edge, respectively. (Baltazar & Falcão de Campos, 2009)

2.2.2 Wake boundary conditions

As shown in Baltazar, Machado, & Falcão de Campos (2011), the two boundary conditions on the wake are: the normal component of the fluid velocity is continuous and equal to the normal velocity of the wake surface , Eq. 28 and the pressure must be continuous across the wake surface, Eq. 29. The first condition, Eq. 28, implies that the vortex sheet moves with the fluid. If $S_W(x,t) = 0$ represents the equation of the vortex sheet surface S_W, then:

$$\frac{\partial S_W}{\partial t} + \vec{\mathrm{V}}^+ \cdot \nabla S_W = \frac{\partial S_W}{\partial t} + \vec{\mathrm{V}}^- \cdot \nabla S_W = 0. \tag{30}$$

Outside of the vortex sheet the Bernoulli equation applies:

$$\frac{\partial \phi}{\partial t} + \frac{p}{\rho} + \frac{1}{2}\left|\vec{V}\right|^2 = \frac{p_\infty}{\rho} + \frac{1}{2}\left|\vec{V}_\infty\right|^2, \tag{31}$$

where p_∞ is the pressure of the undisturbed flow. Applying the Bernoulli equation at a given point on each side of the vortex sheet and subtracting the following expression it is obtained:

$$\frac{\Delta p}{\rho} = -\frac{\partial(\Delta\phi)}{\partial t} - \frac{1}{2}\left(\left|\vec{V}^+\right|^2 - \left|\vec{V}^-\right|^2\right), \tag{32}$$

where $\Delta p = p^+ - p^-$ and $\Delta\phi = \phi^+ - \phi^-$ are the pressure and potential jumps across the sheet, respectively.

From the boundary condition, Eq. 29, the pressure-jump is zero , we obtain from Eq. 32:

$$\frac{\partial(\Delta\phi)}{\partial t} + \vec{\mathrm{V}}_m \cdot \nabla_S(\Delta\phi) = 0, \tag{33}$$

where $\vec{V}_m = \frac{1}{2}\left(\vec{V}^+ + \vec{V}^-\right)$ is the mean velocity and $\nabla_S(\Delta\phi) = \vec{V}^+ + \vec{V}^-$ is the surface gradient of the potential discontinuity, which is equal to the velocity discontinuity on the wake surface. Eq. 33 shows that the potential-jump remains constant following a fluid particle moving on the wake with the velocity $\vec{V}_m$. The Kutta condition states that the velocity must remain bounded at a sharp edge:

$$|\nabla\phi| < \infty. \tag{34}$$

2.2.3 Integral equation

Applying Green's second identity and using the Morino's formulation (Morino & Kuo, 1974), we obtain the integral representation of the perturbation potential at a point p on the body surface:

$$2\pi\phi(p,t) - \iint_{S_B \cup S_H} \left[G(p,q) \frac{\partial \phi}{\partial n_q} - \phi(q,t) \frac{\partial G}{\partial n_q} \right] dS = \iint_{S_W} \Delta\phi(q,t) \frac{\partial G}{\partial n_q} dS \ , \tag{35}$$

where $G(p,q) = -1/R(p,q)$, $R(p,q)$ is the distance between the field point p and the point q on the boundary $S = S_B \cup S_H \cup S_W$. The solution of Eq. 35 determines $\phi(q,t)$ on $S_B \cup S_H$, with $\partial\phi/\partial n_q$ known from Eq. 27. The Kutta condition, Eq. 34, yields the additional relationship between the dipole strength $\Delta\phi(q,t)$ in the wake and the surface dipole strength at the blade trailing edge and is applied in the form of pressure continuity at the trailing edge (Baltazar & Falcão de Campos, 2009).

2.2.4 Velocity, pressure and forces

From the potential flow solution on the surface the velocity components can be calculated by surface differentiation. The pressure coefficient comes from Bernoulli equation and can be written as:

$$C_P = \frac{p - p_\infty}{1/2\rho {U_\infty}^2} = 1 - \left(\frac{|V_t|}{U_\infty} \right)^2, \tag{36}$$

where p_∞ is the pressure of the undisturbed flow, $|V_t|$ is the total velocity and U_∞ is the magnitude of the undisturbed flow velocity.

The inviscid axial force T_i and the torque Q_i on the rotor are calculated from the pressure distribution on the blade surfaces:

$$T_i = \iint_{S_B} p n_x dS, \tag{37}$$

$$Q_i = \iint_{S_B} p(n_y z - n_z y) dS. \tag{38}$$

As in the lifting line theory, the quantities used to express the performance characteristics are the dimensionless power coefficient, axial force coefficient and the Tip Speed Ratio. (Baltazar & Falcão de Campos, 2011)

2.3 Viscous effect

The viscous forces on the turbine blades are calculated using the concept of section lift and drag force that can be derived from two-dimensional lift and drag data.

The inviscid lift force L_i is, per definition, perpendicular to the incoming velocity V to the blade section. The hydrodynamic pitch angle β_i can be determined from the elementary contributions to the ideal axial force dT_i and torque dQ_i by the relation:

$$\tan \beta_i = \frac{dQ_i}{r dT_i}. \tag{39}$$

With viscous effects, the elementary contributions to the axial force and torque are:

$$dT_v = (L_v \cos \beta_i + D \sin \beta_i) dr, \tag{40}$$

$$dQ_v = (L_v \sin \beta_i + D \cos \beta_i) r dr. \tag{41}$$

The viscous lift force L_v (per unit length) of the section is given by:

$$L_v = L_i \frac{C_{L_v}}{C_{L_i}}, \tag{42}$$

where C_{L_v} and C_{L_i} are the section viscous and inviscid lift coefficients of the blade section at the angle of attack α, respectively. The drag force (per unit length) is:

$$D = C_D \frac{1}{2} \rho V^2 c, \tag{43}$$

where C_D is the section drag coefficient at the angle of attack α, and c the section chord. The incoming velocity V can be calculated by the Kutta-Joukowski law in steady flow:

$$L_i = \rho V \Gamma . \tag{44}$$

If viscous corrections on the lift force are ignored C_{L_v}/C_{L_i} is equal to 1 in Eq. 42 The total axial force and torque are obtained by integration of the elementary contributions along the radial spanwise direction. (Baltazar & Falcão de Campos, 2011)

3 Numerical methods and implementation

In this section the numerical methods behind the theory are presented and all the variables in the formulas are non-dimensional.

3.1 Numerical model of the lifting line method

3.1.1 Discretization of the lifting line

The lifting line is a finite vortex where the intensity is changing from hub to the tip. When translating this behaviour in terms of numerical model, the lifting line is discretized in M different smaller consecutive segments with constant value of circulation Γ_i, so the intensity of it will change by steps and not continuously, as shown in Figure 8. The point at the centre of the segments is called control point r_i and the ones that bound them are called end points r_j.

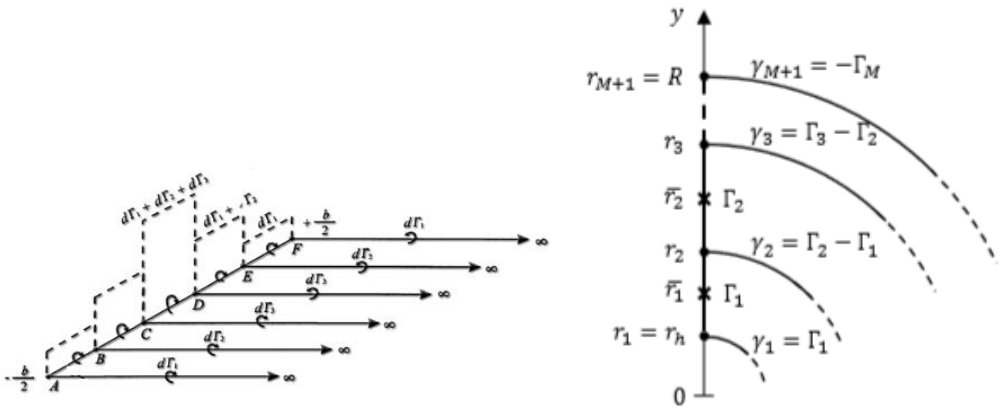

Figure 8: Discretization of the lifting line and circulation.

The segments in which the lifting line is divided have different lengths, the discretization is finer near the hub and the tip because those are the region where the largest gradients of circulation are expected. The distribution of the points follows a half-cosine distribution according to the below shown formula:

$$r_i^* = \frac{1}{2}(1 + r_h) - \frac{1}{2}(1 - r_h)\cos\left(\frac{\pi(i-1/2)}{M}\right),\ i = 1, \dots, M, \tag{45}$$

$$r_j^* = \frac{1}{2}(1 + r_h) - \frac{1}{2}(1 - r_h)\cos\left(\frac{\pi(j-1)}{M}\right),\ j = 1, \dots, M+1. \tag{46}$$

3.1.2 Induced velocities

The induced velocities due to the bound and the trailing vortices come from the Biot-Savart law and they can be written as linear combinations of the circulation as follows:

$$v_{a,t_i} = \sum_{j=1}^{M} C_{a,t_{ij}} \Gamma_j, \tag{47}$$

where M is the number of segments in which the lifting line is discretized.

The $C_{a,t_{ij}}$ are the axial and tangential influence coefficients matrices and they can be computed with two different methods:

- When the wake is helicoidal because the alignment scheme is not applied, it is enough to compute the induced velocities at the lifting line, and this can be done through the analytical expressions of Lerbs (1952);
- When the wake is aligned with the fluid local velocity a numerical integration routine implemented by Melo (2016) can be used. Discretizing the Biot-Savart law it is possible to get the following formula:

$$\vec{v}(x,y,z) = -\sum_{k=1}^{Z}\sum_{i=1}^{M}\frac{1}{4\pi}\left(\int_{r_{j_i}}^{r_{j_{i+1}}}\frac{\vec{e_r}^k\times\vec{R}}{R^3}dr + \int_{L_{j_{i+1}}^k}\frac{\vec{e}_{t_{j_{i+1}}}^k\times\vec{R}}{R^3}ds_{j_{i+1}}^k - \int_{L_{j_i}^k}\frac{\vec{e}_{t_{j_i}}^k\times\vec{R}}{R^3}ds_{j_i}^k\right). \tag{48}$$

  For each control point i, the first integral is the one over each segment of the lifting line and it is solved analytically while the other two integrals are solved numerically, and they consider the trailing vortices shed at the endpoints of the segments. With this method there are no restrictions on the wake geometry, but it takes more time from the computational point of view.

3.1.3 Hub model

The hub behaves as a physical barrier in the secondary flow that tends to move from the lower side of the blade to the upper one, in order to take into account this behaviour it is possible to use an image vortex system to model the hub as an infinite cylindrical wall with radius r_h. As illustrated in (Kerwin, 2001), for each of the $M+1$ trailing vortices an image vortex with symmetrical intensity $\gamma_j' = -\gamma_j$ at the radial position $r_j' = \frac{{r_h}^2}{r_j}$ and wake induced aerodynamic pitch angle:

$$(\tan\beta_i)_j' = (\tan\beta_i)_j\frac{r_j}{r_j'}, \tag{49}$$

is modelled.

Computing the influence coefficients matrices of the image vortex system with the pitch and the radius shown and subtracting them to the ones of the original vortex system the coefficients describing the vortices are found:

$$C_{a,t_{ij}}^{total} = C_{a,t_{ij}} - C'_{a,t_{ij}}. \tag{50}$$

3.1.4 Optimization

The optimization procedure is the one that allows to find the optimum circulation distribution from which the design can be done, choosing a lift coefficient and having the induced velocities distributions. The optimum distribution is the one that leads to the maximum power coefficient C_P for a given loading and two methods to get it are presented.

3.1.4.1 Classical optimization

As already explained in (Sousa, 2018), the optimum circulation distribution with this optimization is obtained when:

$$\frac{(\tan\beta_i)_i}{(\tan\beta)_i} = constant\ (l) \text{ for } i = 1, \dots, M. \tag{51}$$

This condition comes from the assumption that, with inviscid and uniform inflow, the loss of kinetic energy is minimized in the far wake when the conditions $v_a \ll U$ and $v_t \ll \omega r$ (lightly loaded turbines) are satisfied.

The classical optimization system, after manipulating the discrete equations is the following (Sousa, 2018):

$$\sum_{j=1}^{M} \left(C_{a_{ij}} + \frac{\hat{l}}{\bar{r_i}} C_{t_{ij}} \right) \Gamma_j + l\lambda = 1 \text{ for } i = 1, \dots, M, \tag{52}$$

$$C_{T_0} = \frac{2Z}{\pi} \sum_{i=1}^{M} \left\{ \left(\lambda \bar{r_i} + v_{t_i} \right) (1 + \varepsilon_i (\tan\beta_i)_i) \Delta r_i \Gamma_i \right\}, \tag{53}$$

where r_i is the dimensionless radial coordinate of the control point and Δr_i is the length of the lifting line segment i.

The M equations (Eq. 52) allow to find the circulation distribution and the imposed loading C_{T_0}expression (Eq. 53) allows to close to system in order to be able to get the constant l too. The value of C_{T_0} is changed multiple times until the maximum power coefficient C_P is obtained.

3.1.4.2 Lagrange Multiplier Method

Again this method was widely discussed in (Sousa, 2018) and basically it relies on the idea that the optimum circulation distribution, given a certain load, is found imposing the conditions:

$$\frac{\partial \mathrm{H}}{\partial \Gamma_i} = 0 \ \wedge \frac{\partial \mathrm{H}}{\partial l} = 0 \ \text{ for } \ i = 1, \dots, M, \tag{54}$$

to the following equation:

$$H = C_P + l\,(C_T - C_{T_0})\,, \tag{55}$$

where l is called Lagrange multiplier.

Again, after some manipulations of the equations it is possible to get the system (Sousa, 2018):

$$\sum_{j=1}^{M}\left\{\begin{bmatrix}-\lambda\left(1-\frac{\varepsilon_i}{(\tan\beta_i)_i}\right)\left(C_{a_{ij}}\overline{r_i}\Delta r_i + C_{a_{ji}}\overline{r_j}\Delta r_j\right)\\ +\hat{l}(1+\varepsilon_i(\tan\beta_i)_i)\left(C_{t_{ij}}\Delta r_i + C_{t_{ji}}\Delta r_j\right)\\ +\{\lambda(1+\varepsilon_i(\tan\beta_i)_i)\overline{r_i}\Delta r_i\}l\end{bmatrix}\Gamma_j\right\} = -\lambda\left(1-\frac{\varepsilon_i}{(\tan\beta_i)_i}\right)\text{ for } i=1,\dots,M, \tag{56}$$

$$C_{T_0} = \frac{2Z}{\pi}\sum_{i=1}^{M}\left\{\left(\lambda\overline{r_i} + v_{t_i}\right)(1+\varepsilon_i(\tan\beta_i)_i)\Delta r_i\Gamma_i\right\}. \tag{57}$$

The system is solved with an estimation of l and in a iterative way in order to get the optimum circulation distribution and the Lagrange multiplier value.

There is an interesting thing to point out while looking at the system, in fact the first set of equations can be written as:

$$\sum_{j=1}^{M} M_{ij}\Gamma_j = B_i, \tag{58}$$

Where:

$$M_{ij} = -\lambda\left(1-\frac{\varepsilon_i}{(\tan\beta_i)_i}\right)\left(C_{a_{ij}}\overline{r_i}\Delta r_i + C_{a_{ji}}\overline{r_j}\Delta r_j\right) + +\hat{l}(1+\varepsilon_i(\tan\beta_i)_i)\left(C_{t_{ij}}\Delta r_i + C_{t_{ji}}\Delta r_j\right), \tag{59}$$

$$B_i = -\lambda\left(1-\frac{\varepsilon_i}{(\tan\beta_i)_i}\right)\overline{r_i}\Delta r_i - \lambda l(1+\varepsilon_i(\tan\beta_i)_i)\overline{r_i}\Delta r_i. \tag{60}$$

And in the case of inviscid fluid ($\varepsilon = 0$) it gets:

$$M_{ij} = -\lambda\left(C_{a_{ij}}\overline{r_i}\Delta r_i + C_{a_{ji}}\overline{r_j}\Delta r_j\right) + \hat{l}\left(C_{t_{ij}}\Delta r_i + C_{t_{ji}}\Delta r_j\right), \tag{61}$$

$$B_i = -\lambda(1+l)\overline{r_i}\Delta r_i. \tag{62}$$

Dividing all the terms by $-\lambda\overline{r_i}\Delta r_i$, setting $\hat{l} = l$ and considering the following formulas:

$$u_{a_i} = \sum_{j=1}^{M} C_{a_{ij}}\Gamma_j \;\;;\;\; u_{t_i} = \sum_{j=1}^{M} C_{t_{ij}}\Gamma_j\,, \tag{63}$$

$$u_{a_i}{}^{*} = \frac{1}{\overline{r_i}\Delta r_i}\sum_{j=1}^{M} C_{a_{ji}}\overline{r_j}\Delta r_j\Gamma_j \;\;;\;\; u_{t_i}{}^{*} = \frac{1}{\Delta r_i}\sum_{j=1}^{M} C_{t_{ji}}\Delta r_j\Gamma_j\,. \tag{64}$$

It is possible to get the final expression:

$$\frac{1-u_{a_i}-u_{a_i}{}^{*}}{\lambda\overline{r_i}+u_{t_i}+u_{t_i}{}^{*}} = \frac{l}{\lambda\overline{r_i}}\,. \tag{65}$$

This procedure is done following the same procedure of Ribeiro & Falcão de Campos (2003) for propellers. The terms with the star * are related to the transpose influence coefficients matrices so they strictly depend on the wake geometry too. If $u_{a_i}{}^*$ and $u_{t_i}{}^*$ are neglected we must be able to obtain:

$$\frac{\tan\beta_i}{\tan\beta} = -l = const., \tag{66}$$

which is Betz condition of constant pitch and coincides with Lerbs optimum (classical optimization).

Another interesting case is when $u_{a_i}{}^* = u_{a_i}$ and $u_{t_i}{}^* = u_{t_i}$, in fact the equation becomes:

$$\frac{1-2u_{a_i}}{\lambda\bar{r}_i+2u_{t_i}} = \tan\beta_{i,far\ \ downstream}, \tag{67}$$

which means that for an optimum turbine the hydrodynamic pitch is constant far downstream from the rotor.

3.2 Numerical model of the panel method

3.2.1 Discretization in the panel method code

As explained in Baltazar & Falcão de Campos (2011) for the numerical solution of the integral eq. 35 we discretise all the surfaces (blades, hub and wake) as in Figure 9 with bi-linear quadrilateral elements which are defined by four points on the body surface. The grid on the blade and hub and the initial grid on a rigid wake is generated by a ProPanel code.

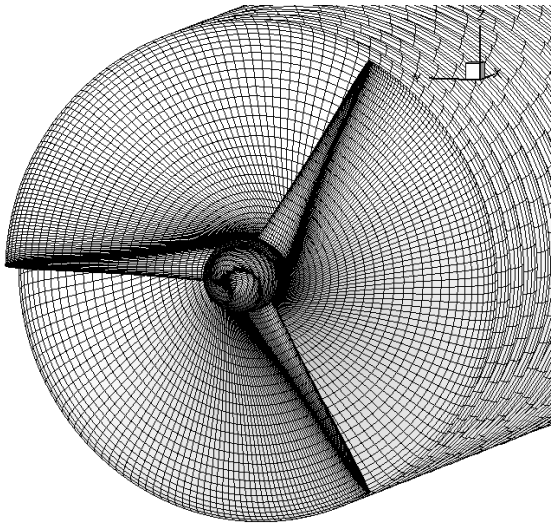

Figure 9: Discretization of hub, blades and wakes from ProPanel code.

The turbine blade surface is discretised in the spanwise radial direction by a set number of strips, extending chordwise from the blade leading edge to the trailing edge. Cosine spacing in the radial and chordwise directions is used.

For the discretisation of the hub surface an elliptical grid generator is used, it is necessary to set the pitch at the connection point between the hub and the blade, the axial coordinate of the first and last panel, the number of panels upstream and downstream.

The blade wake surface is discretised in the spanwise direction extending downstream from the trailing edge the corresponding strips on the turbine blade previously defined. The pitch both at the trailing edge and at the ultimate wake section is set as the aerodynamic pitch coming out from the design conducted through the lifting line code and the wake obtained is perfectly helicoidal.

3.2.2 Solution of the integral equation

The integral equation 35 is solved in space by the collocation method with the element centre point as collocation point. On the blade and hub surfaces, S_B and S_H, the dipole and source distributions are assumed to be constant on each panel. On the wake surface S_W piecewise linear or constant dipole distributions are assumed, depending on the specific location of the panel.

Let $\mu_j^k = -\phi_j^k$ be the values of the dipole strength of the panel S_n^k on the surface of the k^{th} blade-hub sector, $k = 1, \dots, N$, $j = 1, \dots, N$ and N being the number of panels of each blade-hub sector; let $\mu_{ml}^k = -\Delta\phi_{ml}^k$ be the values of the dipole strengths of the boundary between the panel $S_{m,l-1}^k$and the panel S_{ml}^k of the k^{th} wake, $m = 1, \dots, N_W$, N_{R_w} being the number of panels along the spanwise direction and N_W the number of panels along the streamwise direction of the wake; let σ_j^k be the source strength of the panel S_j^k on the surface of the k^{th} blade-hub sector. If the Equation 35 is exactly satisfied at the central points $P_i, i = 1, \dots, N_P$ of the $N_P = N \times$ panels on the K surface of the K blade-hub sectors, we obtain a system of algebric equations in the form:

$$\sum_{k=1}^{K}\sum_{j=1}^{N}\left(\delta_{ij} - D_{ij}^k\right)\phi_j^k - \sum_{k=1}^{K}\sum_{m=1}^{N_{R_W}}\sum_{l=1}^{N_W} W_{iml}^k \Delta\phi_{ml}^k = -\sum_{k=1}^{K}\sum_{j=1}^{N} S_{ij}^k \sigma_j^k, \;\; i = 1, \dots, N_P \,, \tag{68}$$

in which δ_{ij} is the Kronecker delta and D_{ij}^k and S_{ij}^k are the influence coefficients given by:

$$D_{ij}^k = \frac{1}{2\pi}\iint_{S_j^k} \frac{\partial}{\partial n_q}\left(\frac{1}{R(p_i,q)}\right) dS, \tag{69}$$

$$S_{ij}^k = \frac{1}{2\pi}\iint_{S_j^k} \frac{1}{R(p_i,q)}\, dS, \tag{70}$$

and W_{iml}^k is a wake influence coefficient which may be written as a linear combination of elementary integrals of the dipole type. The influence coefficients are determined analytically using the formulations of (Morino & Kuo, 1974). The source strength σ_j^k is determined from the boundary condition (Eq. 27) as:

$$\sigma_j^k = -\vec{n}_j^k \cdot \vec{V}_\infty\left(r_j^k, \theta_j^k\right), \tag{71}$$

where $\vec{n}_j^k$ is the unit vector at the control point $\left(x_j^k, r_j^k, \theta_j^k\right)$ of the k^{th} blade. To reduce the dimension of the system of equations the boundary condition is only applied at the key blade $k = 1$. Hence, the contributions of the other blades ($k > 1$) are assumed to be known when solving for the key blade. Furthermore, only the first strip of dipoles in the wake close to the trailing edge of the key blade is treated as being part of the unknowns.

The integral equation is solved by using the in-house IST panel code PROPAN that requires as input the geometry of the blades, the hub and the rigid wake coming out from the ProPanel code mentioned before, plus an input file. In particular, in the input file those information need to be specified: the number of wake alignment iterations, the number of sections in which the alignment is done and their axial coordinates, the tolerances for the computation of the induced velocities, the number of panels for one revolution of the wake and so on.

The output of the code is the wake geometry aligned with the local velocity, the circulation distribution, the thrust and power coefficients. Moreover, using a post processing code the pressure distribution in any blade section and the aerodynamic pitch at any sections are found. (Baltazar & Falcão de Campos, 2009)

3.2.3 Numerical Kutta condition

The value of the dipole strength at the blade trailing edge $\Delta\phi$ is determined by the application of a Kutta condition. An iterative pressure Kutta condition is applied stating that the pressure is equal on the collocations points of the panels of the two sides adjacent to the trailing edge. At this point, the non-linear system of equations can be solved applying the method of Newton and Raphson, as it is done in this work, and the dipole strength at the blade trailing edge is found.

3.3 Computational procedure

In this section the design computational procedure is shown (Figure 10). The first flow chart shows the outer cycle, the one that beside containing the lifting line design contains the wake alignment done with the panel method too.

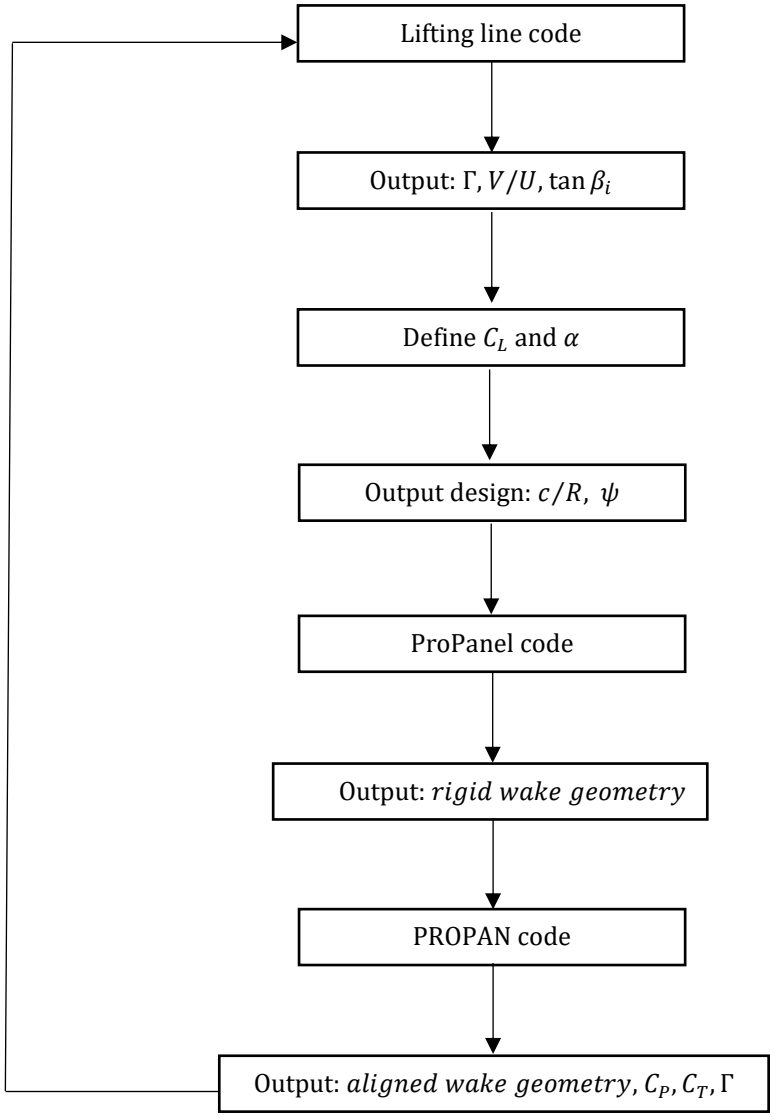

Figure 10: Flow-chart of the outer cycle.

The second flow-chart (Figure 11) shows with more details how the lifting line code is built , the iterations within it and the convergence expected. The contents of the two flow charts and how they are combined is explained in the following pages.

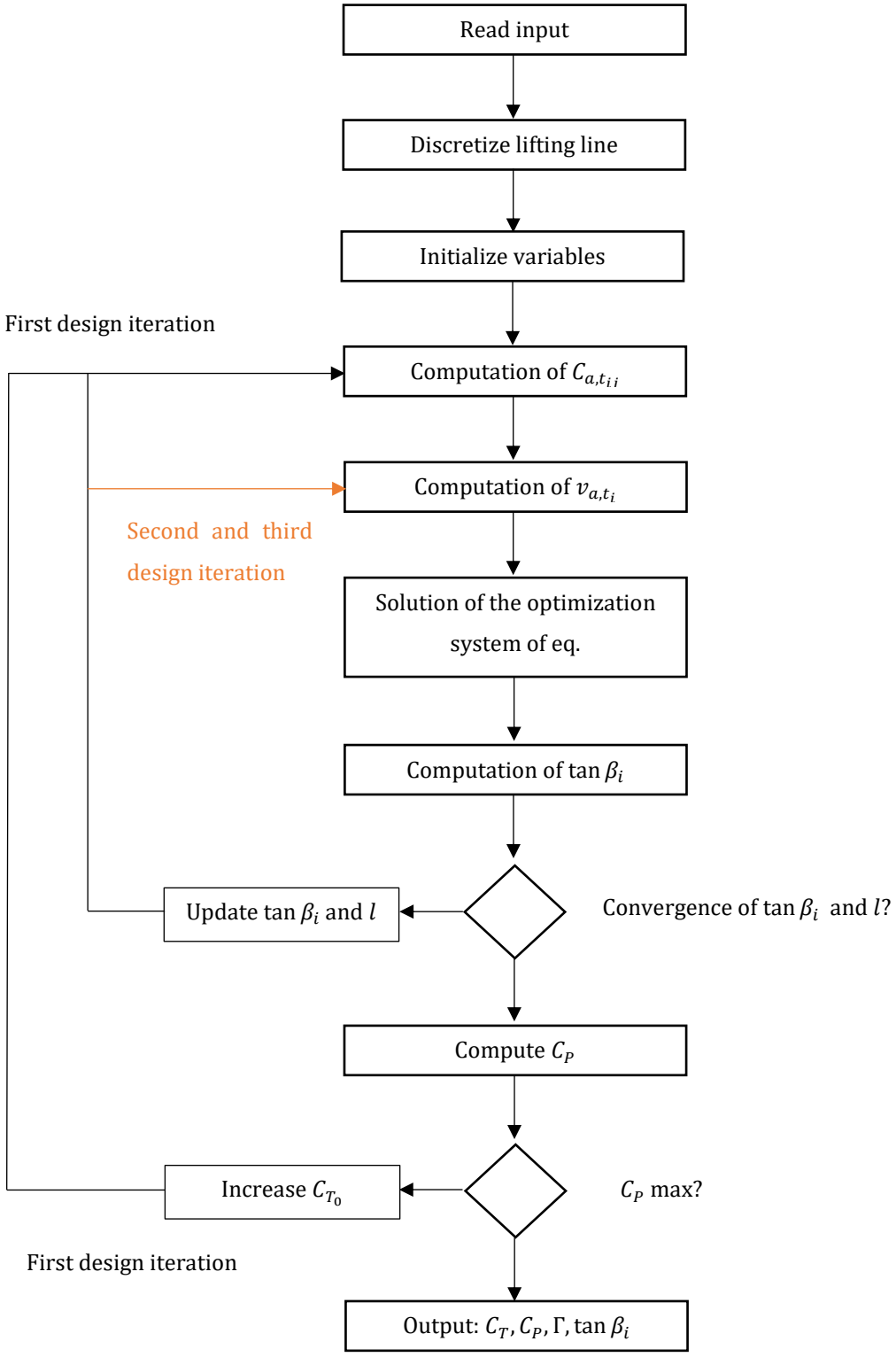

Figure 11: Flow-chart of the lifting line design procedure.

In the lifting line code (Figure 11) the inputs are provided through an editable text file. Among the specified parameters there are the number of blades, the tip speed ratio, the drag to lift ratio, the optimization method used, the thrust coefficient and the information related to the discretization and the numerical computations. The lifting line is then discretized as previously explained. All the variables of the code are then declared and set equal to zero and the induced aerodynamic pitch angle is assumed equal to the undisturbed aerodynamic pitch angle (considering $v_{a,t} = 0$):

$$\tan\beta_i = \tan\beta = \frac{1}{\lambda r} \tag{72}$$

For our purpose, the wake alignment is not used through the lifting line theory, that is why the wake geometry is defined based on $\tan\beta_i$ at the lifting line (helicoidal wake with constant pitch along the x axis) at the first main cycle iteration. Through the analytical expression of Lerbs (1952) the influence coefficients matrices $C_{a,t_{ij}}$ are defined and the computation of the induces velocities comes next from Eq. 48. In the first iteration on $\tan\beta_i$ the velocities are zero since the circulation is set equal to zero. The system of equations related to the optimization is then solved (Eq. 52 and 53) and the new values of Γ and l are found. Using Eq. 13 the aerodynamic pitch $\tan\beta_i$ is calculated.

The first cycle iteration is almost over but the variables are not optimized or neither converged, that is why $\tan\beta_i$ and l obtained are compared with the previous cycle. If the difference is lower than a tolerance set through the input text file, the variables are considered converged otherwise the values of the two variables have changed (under a relaxation parameter as shown in Eq. 73) and they are used as input in the second iteration:

$$(\tan\beta_i)^{next} = k_N(\tan\beta_i)^{new} + (1 - k_N)(\tan\beta_i)^{previous}, \tag{73}$$

The new value of $\tan\beta_i$ allows to find new values of $C_{a,t_{ij}}$(they only depend on the wake geometry) and $v_{a,t}$ (using Γ obtained in the previous cycle). Later, solving again the system of equations (Eq. 52 and Eq. 53) , Γ and l are computed and eventually a new value of $\tan\beta_i$ is obtained.

The iterations stop when the conditions in Eq. 74 are satisfied:

$$\left|\frac{(\tan\beta_i)_i^{new} - (\tan\beta_i)_i^{previous}}{(\tan\beta_i)_i^{new}}\right| < \varepsilon_N \ \wedge \ \left|\frac{l^{new} - l^{previous}}{l^{new}}\right| < \varepsilon_N. \tag{74}$$

The variables are now converged, and the power coefficient is found from Eq. 22. However, the optimization process is not over yet, in fact it is known that the optimum design comes from the optimum circulation distribution that corresponds to the highest power coefficient possible, based on a certain loading. The thrust coefficient C_T (representing the imposed loading) is changed as input and the code is let to run until the highest C_P is found.

The design begins now: once the optimum circulation distribution is found a wind turbine airfoil must be chosen to work on. In our case the profile S809 was chosen and based on the lift to drag distribution with the angle of attack α, it is possible to choose the lift coefficient of the blade section.

In particular, the lift coefficient distribution is provided for both inviscid and viscous case while the drag coefficients for the viscous case only (since it would be zero in the inviscid one). When the design is based on the assumption of inviscid fluid, a spline of the lift to drag coefficient is interpolated (see Figure 21) from the viscous data and once the maximum ratio and the corresponding angle of attack are found, it is possible to get the lift coefficient of the blade section (see Figure 22) from the inviscid flow lift coefficient distribution.

The angle of attack along the radial coordinate and the lift coefficient are now defined and from the formula below the chord c is obtained:

$$c = \frac{2\Gamma}{C_L V}. \tag{75}$$

The pitch ψ is obtained from Eq. 14 where all the variables are non-dimensional and the velocity is calculated from Eq. 15.

Looking at Figure 10, we are now at the ProPanel code step, in which a rigid perfectly helicoidal wake geometry is created, based on some information provided such as:

- Radial chord distribution;
- Radial blade pitch distribution;
- Radial skew distribution;
- Radial rake distribution;
- Geometry of the blade section;
- Geometry of the hub;
- Geometry of the wake (based on the pitch distribution);
- Number of panels in the radial direction;
- Stretching parameters for the grid construction.

This preliminary geometry is used as input of the panel method code, in which the analysis of the rotor happens. An input file specifying the flow conditions must be filled, it contains many information among which, the axial coordinate in which the wake must be aligned with the local velocity, the number of wake alignment iterations, choice on the Kutta condition, radial strips in which the induced velocities are calculated, panelling characteristics.

After the panel method code is run, the circulation, the thrust and power coefficient and the wake geometry are obtained through some output files. At this point, many attempts are made with a reasonable number of wake alignment sections and iterations (see Convergence analysis) until a solution with a smooth wake geometry is obtained. Through a post processing code, the pitch distributions in different sections downstream and the pressure distribution at different blade radial sections can be plotted and discussed (see Discussion of the results).

The wake geometry is now written in cartesian coordinates and to obtain the lifting line points for the main blade (the one considered along y axis) a transformation in cylindrical coordinates of the trailing edge points with coordinates $(x_{t.e.}, y_{t.e.}, z_{t.e.})$ is made as in Equations 76 – 77 – 78:

$$x_{l.l.} = 0 \ , \tag{76}$$

$$r_{l.l.} = \sqrt{{y_{t.e.}}^2 + {z_{t.e.}}^2}, \tag{77}$$

$$\varphi_{t.e.} = 0. \tag{78}$$

Then the cartesian lifting line coordinates are found (see Equations 79 - 80 - 81):

$$x_{l.l.} = 0 \ , \tag{79}$$

$$y_{l.l.} = r_{l.l.} \ , \tag{80}$$

$$z_{l.l.} = 0 \ . \tag{81}$$

The computations shown have to be done for every radial sequence of wake points, in this way the format of the wake can be read by the lifting line code. The lifting line optimization can now be repeated reading the wake geometry from an editable file and assuming the same optimum thrust as in the first design. Furthermore, the way the influence coefficients matrices are found is different since the wake will not be perfectly helicoidal, in fact a numerical integration routine is used. The radial end points used in this iteration of the lifting line code do not follow a half-cosine distribution but depend on the wake geometry found through the panel method code and the control points are still the mid-point of every single lifting line segments. The main difference in this second use of the lifting line lies in the fact that the wake geometry does not follow any perfect helicoidal shape as before, the influence coefficients matrices $C_{a,t_{ij}}$ do not change with $\tan\beta_i$ because the geometry is rigid and they are not found from the analytical integration of Lerbs but with the numerical one. The $\tan\beta_i$ and l keep changing in order to solve the classical optimization system, therefore the cycle on $\tan\beta_i$ still need to be kept in this optimization procedure. With the updated circulation distribution the design can be repeated in the exact same way as already done the first time and keeping the same lift coefficient and angle of attack. When the chord and the blade pitch distributions are calculated, ProPanel and PROPAN codes allow to find a new wake geometry that will be used as input in the next lifting line design, using the same thrust coefficient as the one found in the first lifting line design. This entire outer cycle is repeated two times, every time adapting the design of the blade made with the lifting line method to the wake geometry obtained with the panel method code.

For the viscous design the process is exactly the same, with the difference that the drag to lift ratio is set equal to 0.011 (reciprocal value of the lift to drag ratio value of 89.6) in the lifting line code and the lift coefficient C_L and the angle of attack α are different from the ones used in the inviscid design.

3.4 Convergence analysis

Numerical methods like the ones used in the lifting line theory and the panel methods inevitably bring some errors with them:

- Round off error, due to inexactness in the representation of real numbers and the arithmetic operations done with them;
- The iterative error, which comes from a finite number of iterations of a specific method and it is related to a set tolerance;
- The discretization error, related to the number of elements used to discretize the blade, the lifting line and the wake.

In (Sousa, 2018) it is shown how the effect of the discretization in the lifting line code affects the power coefficient, the circulation and the induced aerodynamic pitch distributions. Based on his work it is possible to conclude that the discretization error becomes negligible for our purposes when the number of lifting line elements is 30 so it was decided to use this number for the computation of the variables aforementioned. Thus, the following discussion on the errors is based on the in-house IST PROPAN code. The circulation distribution, the optimum loading and the power coefficient are the variables computed for the analysis. Moreover, the geometry of the wake is continuously monitored through the software TecPlot in order to obtain the smoothest geometry possible to be used in the lifting line code as input.

3.4.1 Wake alignment sections

It was decided to start the analysis choosing a number of combinations of sections and making them run in the panel code with a fixed high number of wake alignment iterations. The initial grid used as input for the panel method code is always the same one, therefore only the number of sections in which the alignment is done is changing. The results are summarized in Table 1.

# of wake alignments sections	**Example of combinations {x/R}**	**C_T**	**%variation**	**C_P**	**%variation**
2	{0,1}	0.7231		0.4636	
3	{0,0.5,1}	0.7624	5.44%	0.5079	9.55%
4	{0,0.05,1,2}	0.7999	4.92%	0.5538	9.04%
5	**{0,0.05,0.2,1,2}**	**0.8097**	**1.22%**	**0.5658**	**2.16%**
6	{0,0.05,0.1,0.2,1,2}	0.8097	0.00%	0.5656	-0.03%
7	{0,0.05,0.1,0.2,0.3,0.4,0.5}	0.8097	0.00%	0.5656	0.00%
8	{0,0.05,0.1,0.2,0.3,0.4,0.5,1}	0.8099	0.02%	0.5659	0.04%
9	{0,0.05,0.1,0.2,0.3,0.4,0.5,0.6,1}	0.8106	0.09%	0.5667	0.14%

Table 1: Thrust and power coefficients varying the number of alignment sections.

The variations of the optimum thrust coefficient and power coefficient become quite low (and reasonable for our purposes) once the number of alignment sections exceeds five (see Figure 12, Figure 13). As highlighted in the table the combination of sections chosen to work on is {0, 0.05, 0.2, 1, 2} and the smoothness of the geometry is confirmed by drawing that in TecPlot (Figure 30 and Figure 31)

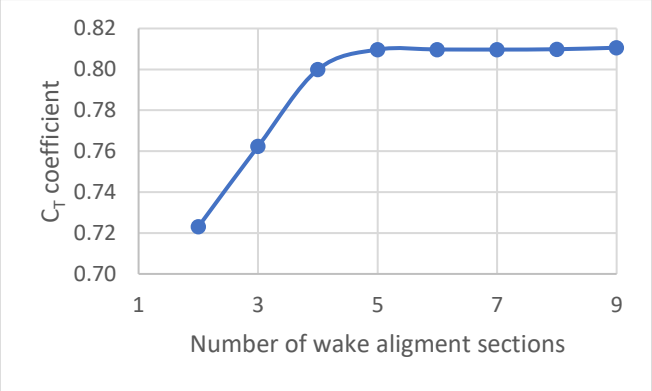

Figure 12: Convergence of the thrust coefficient varying the number of wake alignment sections.

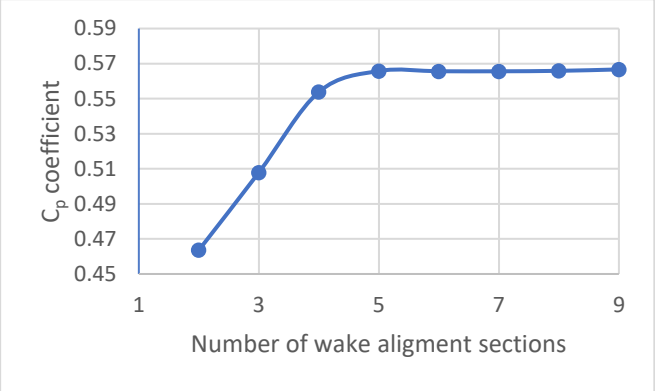

Figure 13: Convergence of the power coefficient varying the number of wake alignment sections.

The circulation distributions (Figure 14) also shows that with a number of sections above five the differences are very small; the zoom graph scale shows differences on the values in the order of 10^{-3}, which is very low and suitable for our purposes.

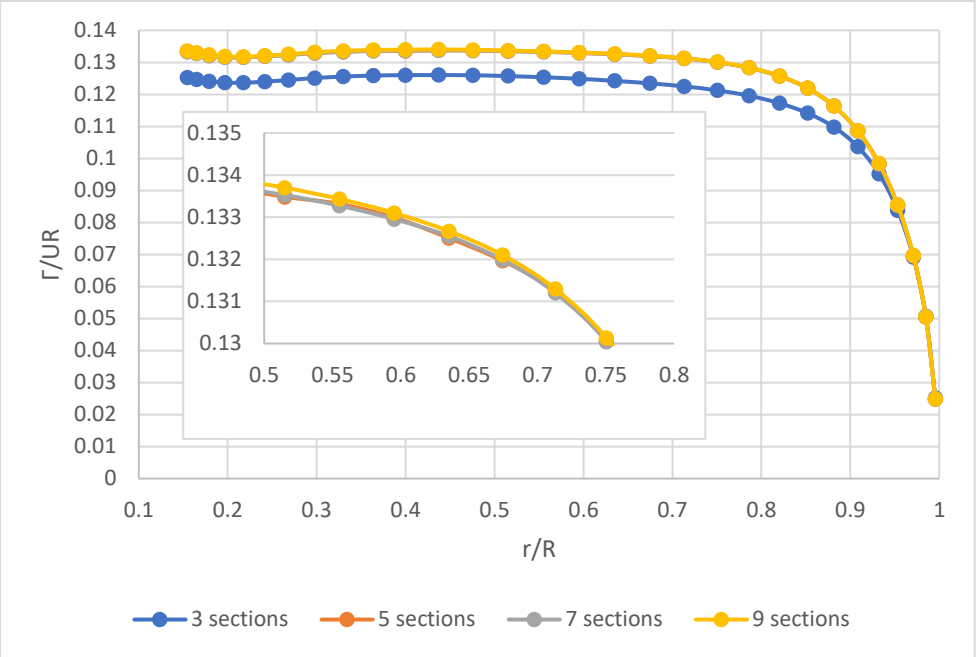

Figure 14: Circulation distributions varying the number of alignment sections.

3.4.2 Wake alignment iterations

After the combination of alignment section is selected, it is now possible to let the panel method code run to get the wake geometry increasing the number of iterations, from 1 up to 11 (as done in the previous section) and see again how the turbine force coefficients change (Table 2).

# of wake alignment iterations	**C_T**	**%variation**	**C_P**	**%variation**
0	0.7808		0.5299	
1	0.7162	-8.27%	0.4573	-13.71%
2	0.7941	10.87%	0.5476	19.75%
3	0.8006	0.82%	0.5547	1.29%
4	0.8106	1.24%	0.5667	2.16%
5	**0.8082**	**-0.29%**	**0.5638**	**-0.51%**
6	0.8073	-0.11%	0.5627	-0.20%
7	0.8094	0.25%	0.5653	0.46%
8	0.8072	-0.26%	0.5626	-0.46%
9	0.8095	0.27%	0.5652	0.45%

Table 2: Thrust and power coefficients varying the number of wake alignment iterations.

Again, for our purposes the differences related to the iteration gets reasonable once the number of iterations exceeds five so it was decided from this moment on to use five as number of wake iterations. This choice makes the computational time faster, although the average computational time is one minute per iteration. In Figure 15, Figure 16 and Figure 17 the trends of thrust coefficient, power coefficient and circulation respectively are shown. The geometry obtained is smooth, so the choice is coherent with the criteria mentioned above (Figure 30 and Figure 31).

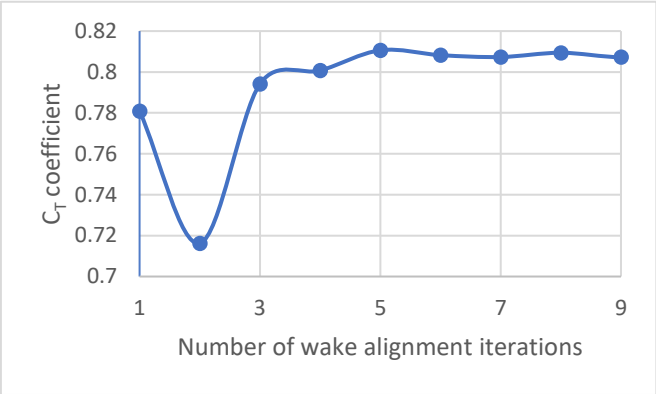

Figure 15: Convergence of the thrust coefficient varying the number of wake alignment iterations.

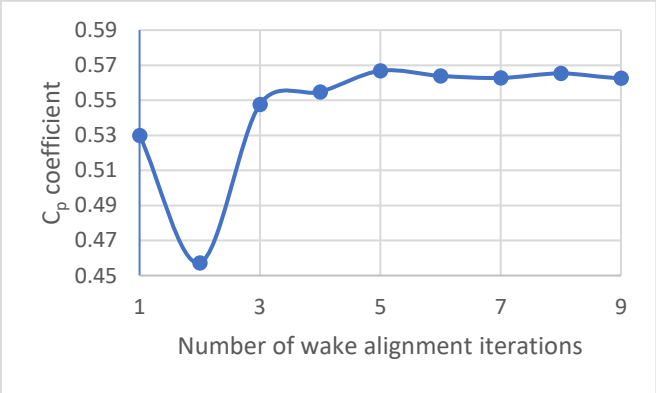

Figure 16: Convergence of the power coefficient varying the number of wake alignment iterations.

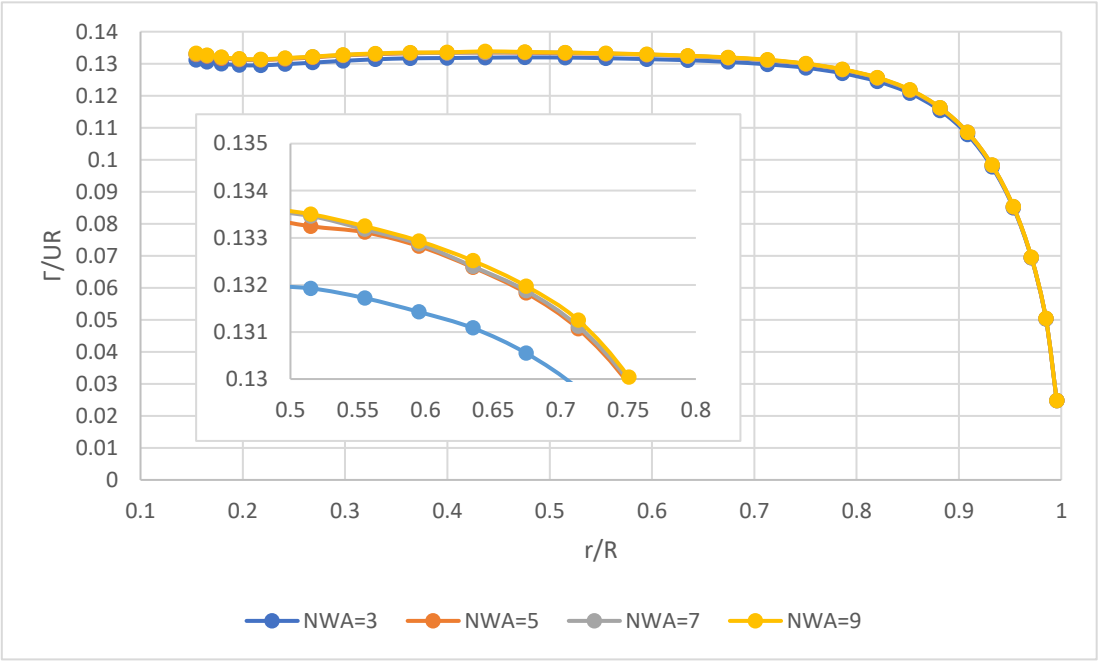

Figure 17: Circulation distribution varying the number of wake alignment iterations.

3.4.3 Number of panels for each revolution

Until now, everything has been done using 40 as number of panels per each revolution of the wake (N θ), taking 14 revolutions of it leading to a wake length of 560 panels (NPW value). It was assumed that 40 is a high enough number of panels for the discretization of the wake but in order to confirm the trustworthiness of this assumption, attempts with lower and higher number of panels were done and the results are shown below in Table 3.

N θ	NPW	C_T	%variation	C_P	%variation
30	420	0.7937		0.5464	
35	490	0.8101	2.07%	0.5663	3.65%
40	**560**	**0.8084**	**-0.21%**	**0.5640**	**-0.41%**
45	630	0.8074	-0.13%	0.5628	-0.22%
50	700	0.8083	0.12%	0.5638	0.18%

Table 3: Thrust and power coefficients varying the number of panels per revolution.

As expected, 40 panels per revolution brings to an acceptable variation on the output results. The thrust and power coefficients in Figure 18 and Figure 19 confirm it and even the circulation distribution in Figure 20 suggest that 40 as number of panels per revolution is a reasonable choice.

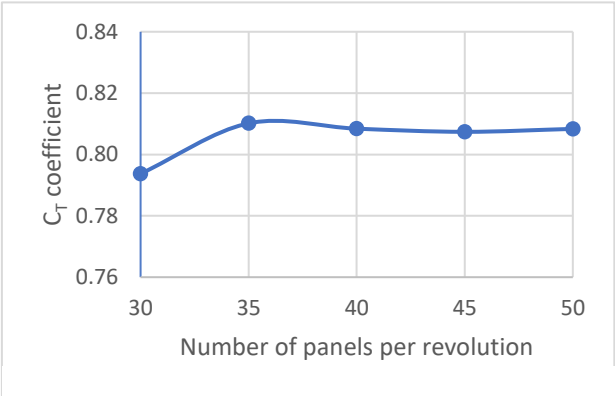

Figure 18: Convergence of the thrust coefficient varying the number of panels per revolution.

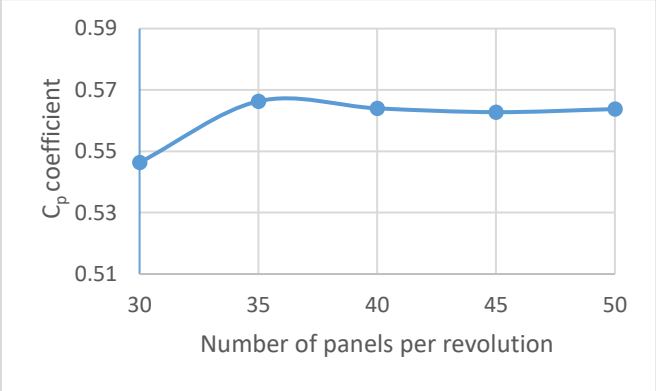

Figure 19: Convergence of the power coefficient varying the number of panels per revolution.

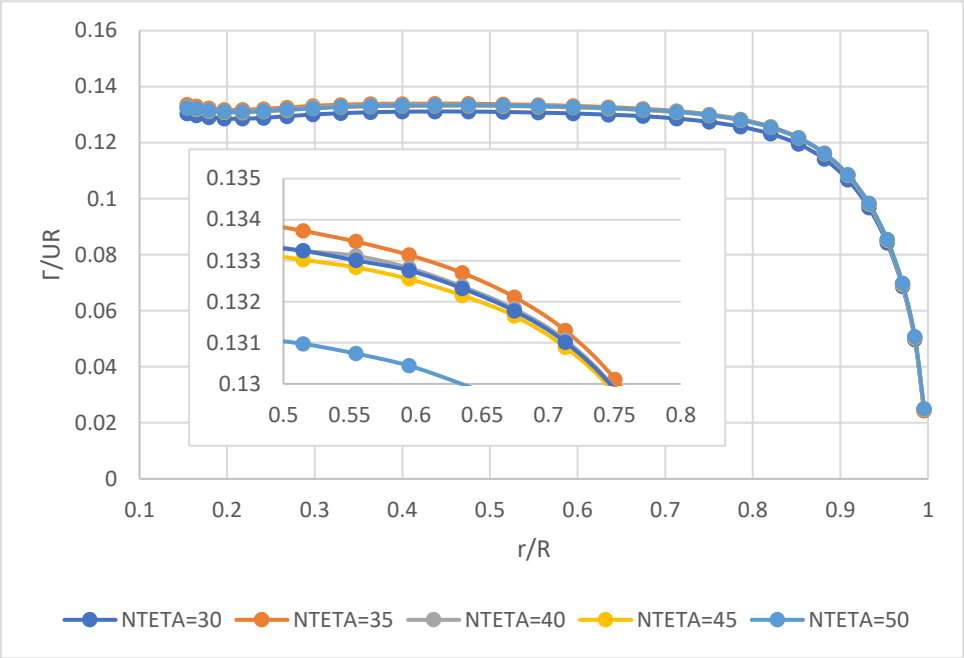

Figure 20: Circulation distribution varying the number of panels per revolution.

4 Discussion of the results

This chapter presents the obtained results, discusses the choice of the lift coefficient in the design done and the difficulties encountered during the computational procedure.

4.1 Choice of the lift coefficient in the design

As explained in Computational procedure one of the most important step in the blade design is the choice of the radial distribution of the lift coefficient. Below the 2D lift to drag ratio of the foil S809 is shown (Figure 21).

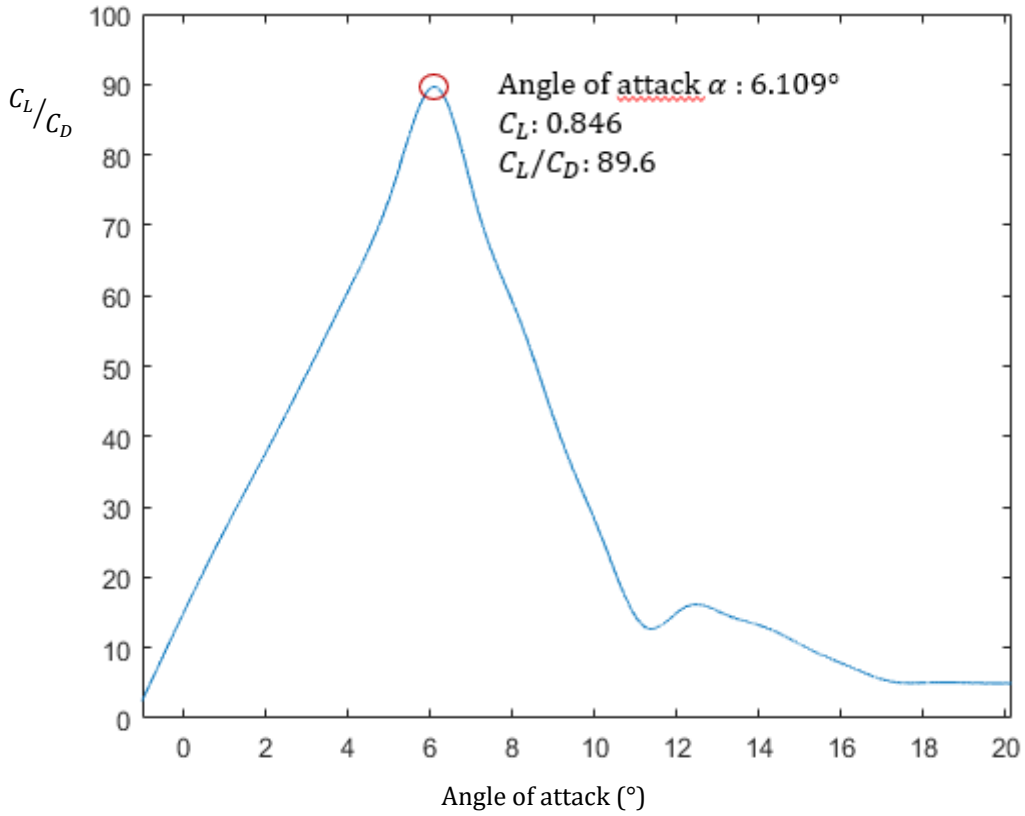

Figure 21: Lift to drag ratio as function of the angle of attack (viscous data).

For the design in the viscous case the lift coefficient is constant along the radius and equal to the one corresponding to the peak of the lift to drag coefficient and same consideration is done for the angle of attack, the reason of this choice is because the comparison of the two designs will not be dependent on the angle of attack.

The choice of the lift coefficient for the inviscid case is based on the lift coefficient corresponding to the angle of attack found for the viscous case and this choice makes sense because it allows a comparison of the

two designs since the angle of attack is kept constant. In Figure 22 the lift coefficient distribution for the inviscid case is shown.

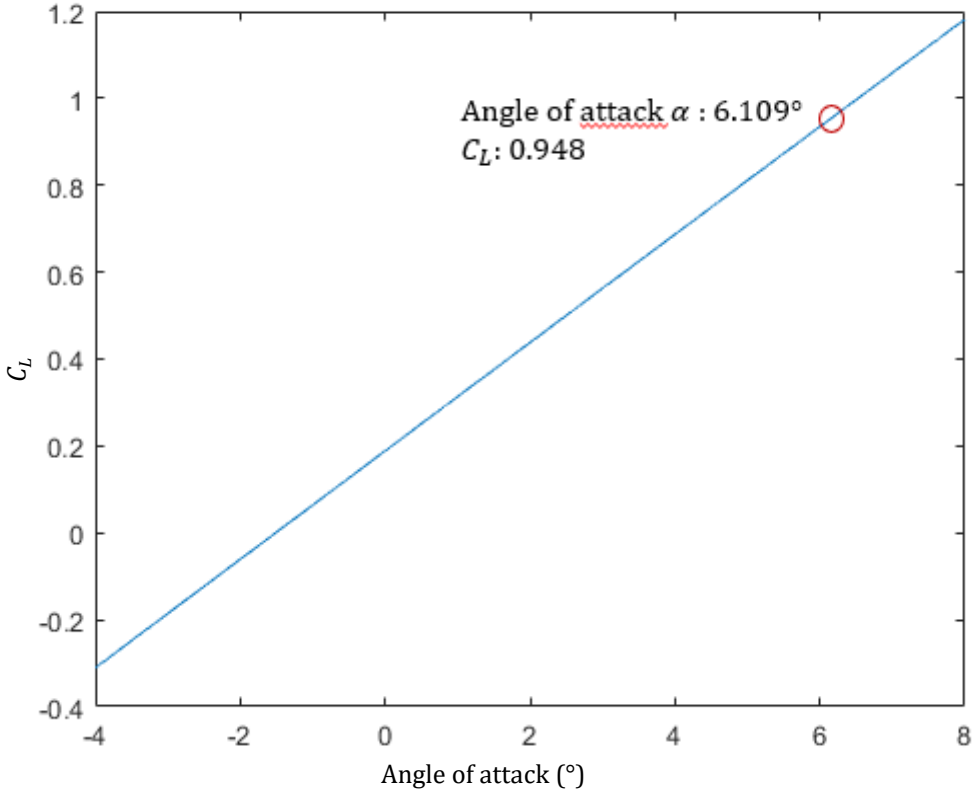

Figure 22: Lift coefficient distribution - inviscid case.

4.2 Approximations and issues in the computational procedure

This section is dedicated to the issues encountered and the approximations needed in the computational procedure.

First of all, it has to be mentioned that the first design with the lifting line code is done with the classical optimization in both the inviscid and the viscous case. Once the results of the blade pitch and chord are obtained, the blade pitch is slightly negative from 70 % of the blade to the tip. The input file in ProPanel does not accept negative pitches of the wake and that is why it is changed to slightly positive through an interpolation. This choice might influence negatively the shape of the wake, giving some distortions in it.

Indeed, a problem encountered while running the panel method code to obtain the aligned wake is indeed the geometry itself. In fact, for most of the alignment sections combinations at around 60% of the blade length the geometry obtained shows distortions (Figure 23) from the smooth geometry we aim at. In order to overpass this issue five strips in which the induced velocities are calculated are removed, increasing the interpolation errors. This choice leads to a smoother geometry without changing the circulation, thrust and power coefficients. The panel method code was run with different combinations of strips taken out and the

smoothest geometry was considered the one to use in the new design with the lifting line code. The same kind of procedure is also done in the second outer cycle, when the wake is aligned for the second time.

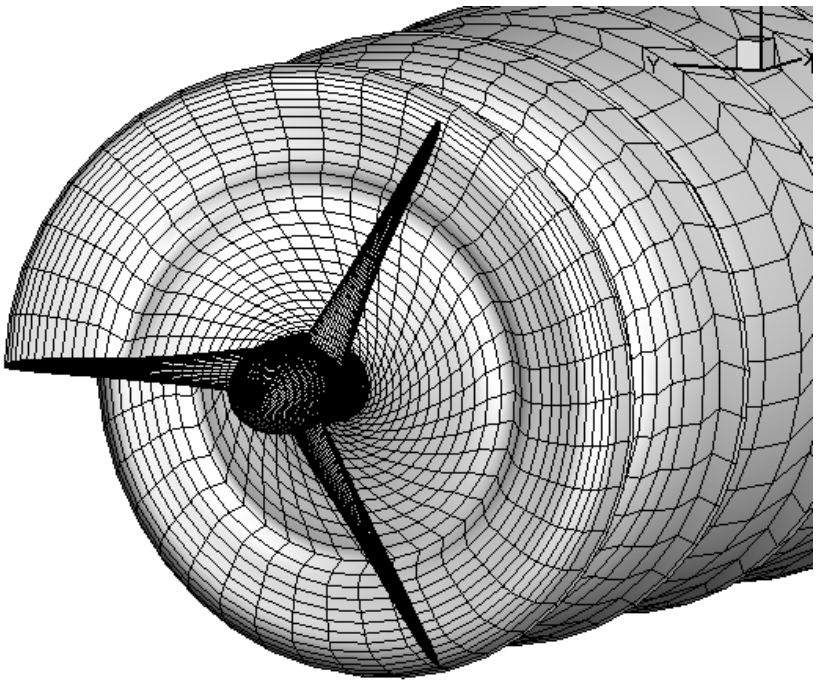

Figure 23: Distortions in the aligned wake geometry - inviscid case.

Another issue encountered relies on the second and third design for both inviscid and viscous case. In fact, the idea was to use in those cases the Lagrange multiplier method that would bring to more accurate results as proven by (Sousa, 2018) a but the distribution calculation obtained was not smooth (see Figure 24 for the inviscid case).

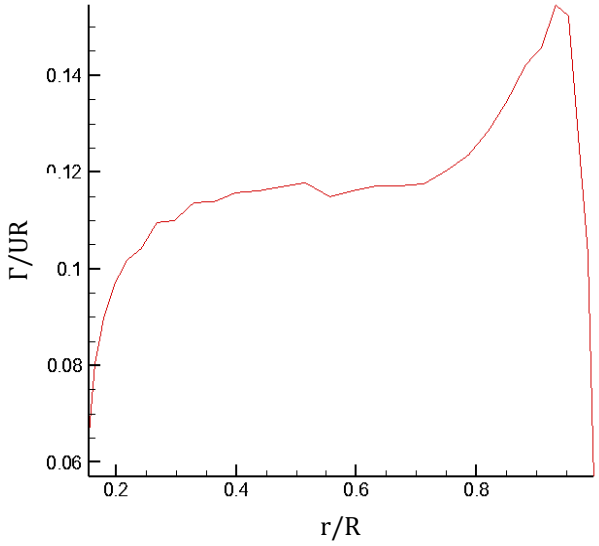

Figure 24: Circulation distribution with Lagrange multiplier method.

It is difficult to state the exact reason why the circulation distribution turns in such a way when the aligned wake geometry obtained with the panel code is used as input in the lifting line one. However, it was found out that the problem lies on the transpose of the influence coefficients matrices. As a matter of fact, when those ones are set to zero (classical optimization condition for the inviscid case) the circulation distribution is smooth (Figure 25 for the inviscid case). The transpose matrices are linked to the term of induced velocity with the star * in equation 65.

Since the Lagrange multiplier method faces these problems it was decided to proceed using the classical optimization in the second and third design iteration for inviscid and viscous case.

4.3 Inviscid results

In Figure 25 the optimum circulation distributions for the three different design iterations done with the lifting line code are shown. It is possible to see that the second and third design distributions are very similar and at the tip the value falls to zero and at the hub the value is finite, in agreement with the theory (Anderson, 2001). The value of the circulation falls drastically down at around 80% of the blade length. It has to be mentioned that the circulation distribution shown is obtained with the classical optimization which relies on the assumption of lightly loaded turbines. The main difference between the classical optimization and the Lagrange multiplier method, in the case of $\varepsilon = 0$, is found in the transpose influence coefficient matrices; in fact, when those terms are set equal to zero the Lagrange multiplier method gives the same system of equations as the classical one (Ribeiro & Falcão de Campos, 2003).

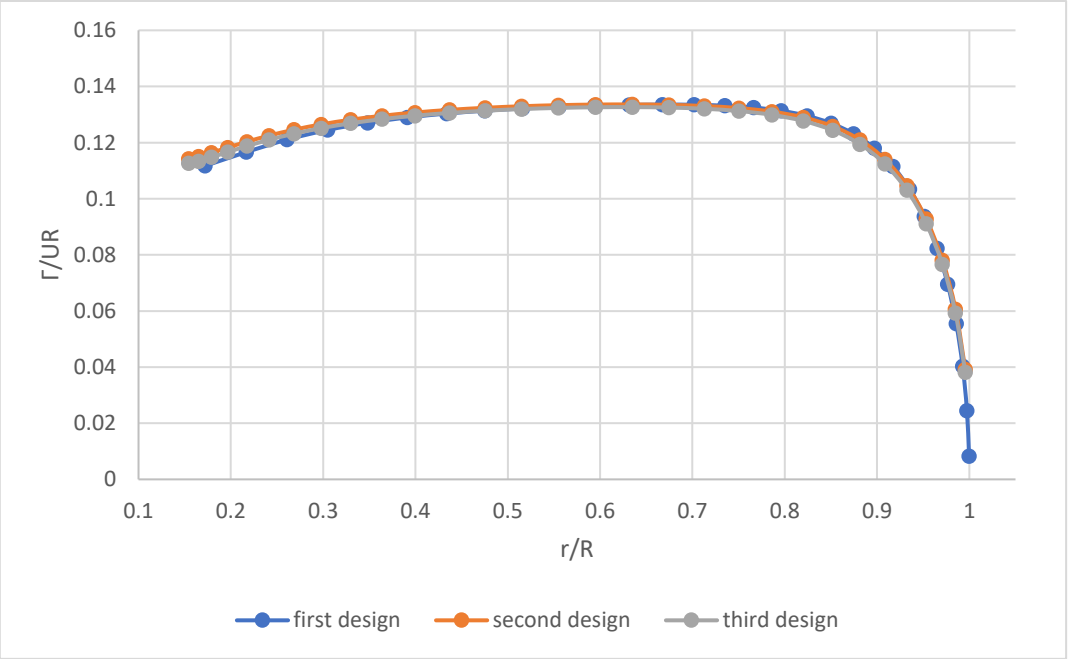

Figure 25: Circulation distribution – inviscid case.

The distribution shows good agreement with Sousa's and this suggests that there are not many remarkable differences in the results of the optimized circulation.

From the circulation distribution the design is done choosing the lift coefficient and the dimensionless pitch and chord distributions are obtained.

The plot in Figure 26 shows the radial distribution of the blade pitch and again, as it happens with the circulation, the second and the third design give similar results. The pitch falls down with a hyperbolic trend, the trend is understandable looking at the triangle of velocities shown in Theory. Looking at the graph it is possible to notice that the differences in terms of pitch values get lower when going from the second design to the third one. In fact, the differences between the first and second design exceeds 10% but from the second to third design they get lower, around 2%, expect in the region close to tip where they get again around 10%.

Looking at the Figure 27 the dimensionless chord distribution is shown. The distribution strongly depends on the circulation distribution and the velocity at the denominator. The chord goes to zero at the tip and this makes sense because even the circulation falls to zero there. The differences in terms of chord are already very low from the first to second design and when moving to the third design they get to values lower than 1%.

The differences of chord and pitch discussed suggest the convergence of the design reached, this will be confirmed later with the discussion of the power coefficients.

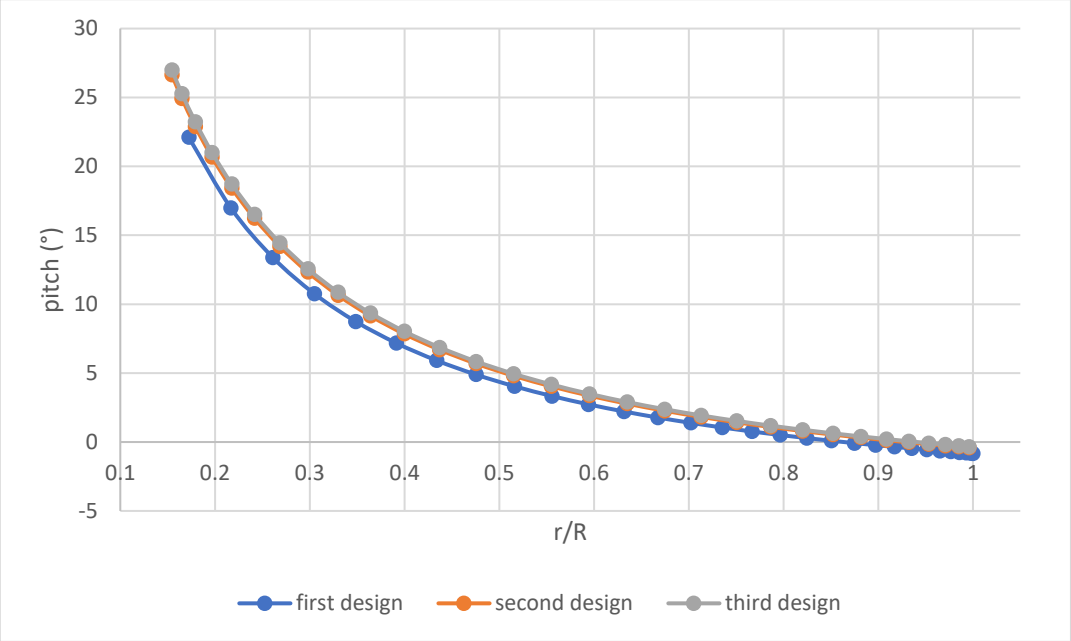

Figure 26: Blade pitch – inviscid case.

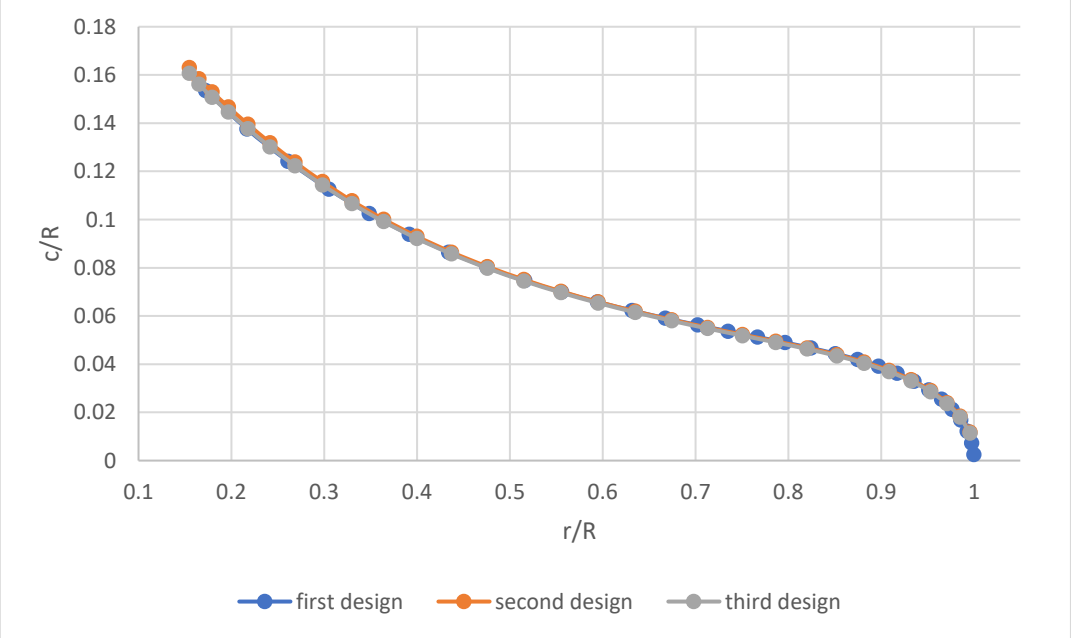

Figure 27: Chord – inviscid case.

Table 4 shows the thrust and power coefficients obtained with the lifting line code and the panel method one. The thrust coefficient is kept constant in the lifting line code every time the design is re done, and equal to the one obtained with the first design. However, looking at the panel method code coefficients for the second cycle the thrust coefficient falls slightly down, those differences come from the fact that the wake is analysed with the panel code while the optimization procedure is done with the lifting line method.

Although there are differences between the power and thrust coefficients when moving from the lifting line code to the panel code, our main interest is to observe how the thrust and power coefficients obtained with the lifting line code change. It is necessary to point out that the power coefficient show convergent behaviour when moving from the second cycle to the third one. It is interesting to discuss the effect of aligning the wake while keeping the thrust coefficient constant: when the wake is not aligned as in the first iteration the power coefficient is 0.52, but already after one iteration of alignment of the wake it gets to 0.56, increasing of almost 10%.

Lifting line code	**Panel method code**
$C_T = 0.804$ $C_P = 0.520$	$C_T = 0.808$ $C_P = 0.564$
$C_T = 0.804$ $C_P = 0.560$	$C_T = 0.771$ $C_P = 0.555$
$C_T = 0.804$ $C_P = 0.562$	

Table 4: Thrust and power coefficients – inviscid case.

The two circulation distributions obtained through panel method code do not really matter to us, as the design is eventually made from the optimized distributions coming from the lifting line code. However, it is interesting to see the shape of those: it is possible to see that the differences between the first and second cycle are small and when the blade radius exceeds 90% of the radius length the graphs overlap. The main difference between these distributions and the ones obtained with the lifting line method (Figure 28) is in the region close to the root of the blade (when the ratio r/R is lower than 40%), where the values do not go significantly down as it happens with the lifting line method.

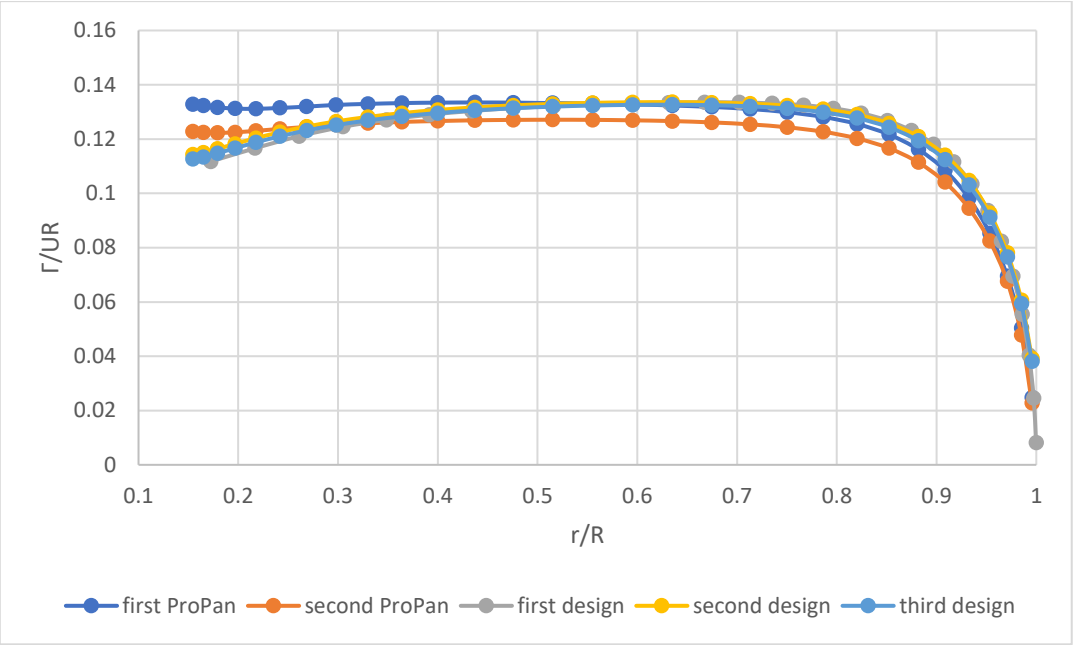

Figure 28: Comparison with the circulation distribution from PROPAN – inviscid case.

The wakes obtained through the first, second and third design are shown in Figure 29, Figure 30 and Figure 31 . The first wake (Figure 29) is perfectly helicoidal, as it is not aligned and the pitch is uniform everywhere along the x direction and equal to the β_i obtained from the lifting line distribution. The second wake (Figure 30) is already aligned and there it is possible to see the wake folding in the downstream direction at any axial alignment section, which is the right expected behaviour for a turbine. In fact, Sousa tried many alignment section combinations and whenever the convergence was obtained the wakes did not show the right folding close to the rotor plane, folding upstream. The radial expansion is not taken into account in this model therefore the radial coordinates of the trailing vortices remain constant.

The third wake (Figure 31) shows the same behaviour as the second one. The differences between the second and third wakes are not remarkable from the graphs but they lead to similar chord and pitch distributions.

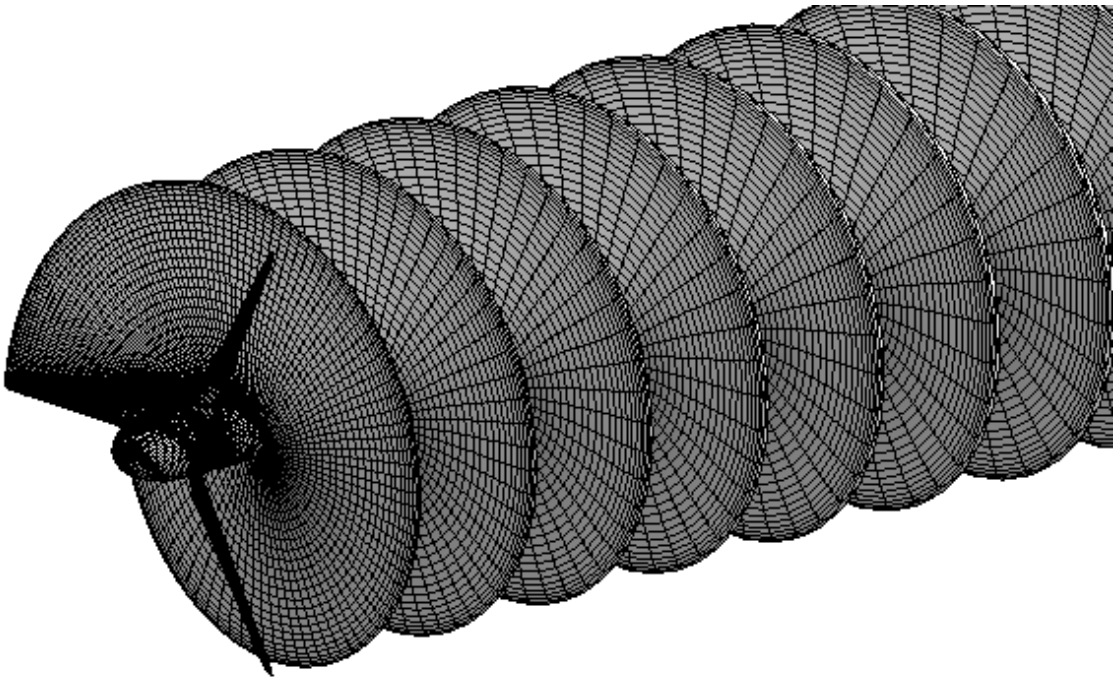

Figure 29: Helycoidal wake – inviscid case.

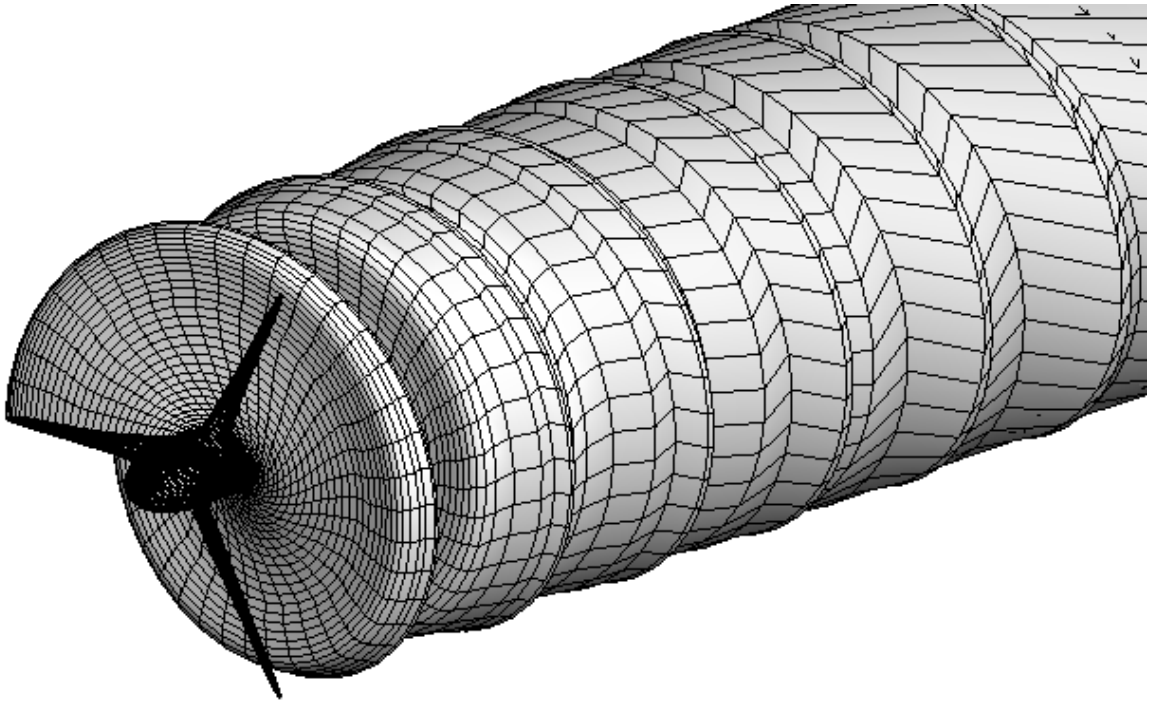

Figure 30: First aligned wake – inviscid case.

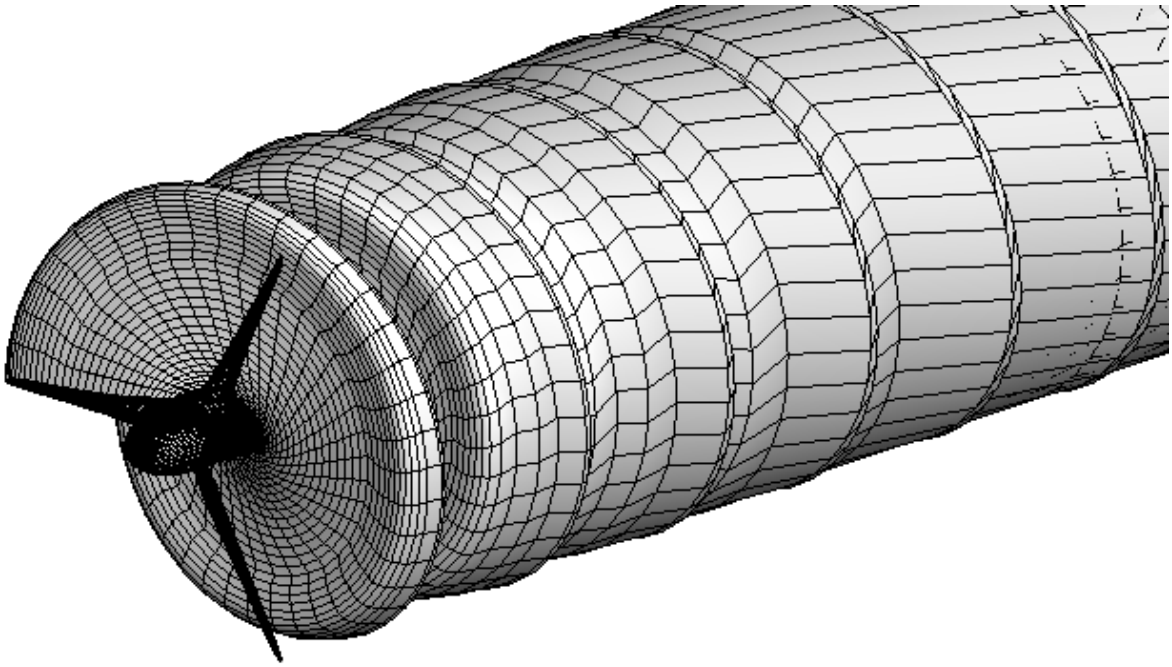

Figure 31: Second aligned wake – inviscid case.

To prove the folding behaviour from a more analytical point of view, a post processing code that uses the wake as input and give the pitch distribution as output is used. The distribution of the pitch at the lifting line is obtained through the lifting line optimization and it is constant since the optimization procedure used is the classical one. When looking at the distributions at different axial sections (Figure 32) it is possible to see that the pitch increases while getting close to the tip, unlike Sousa's results where in the sections close to the rotor plane the pitch decreased when approaching the tip. The yellow line in the graph, unlike the orange and grey ones, shows that the behaviour of the pitch tends to be constant from 15% to 80% of the blade length at the alignment section $^{x}/_{R} = 1$.

Looking at the same alignment sections chosen by Sousa in Figure 33 it is possible to conclude that numerical values show good agreement with our results but the trend is different in the region close to the blade tip at the axial section $^{x}/_{R} = 0$ and $^{x}/_{R} = 0.25$, this suggests that our wake alignment results are more reliable because the trend is the typical one for turbines (Baltazar et al., 2011).

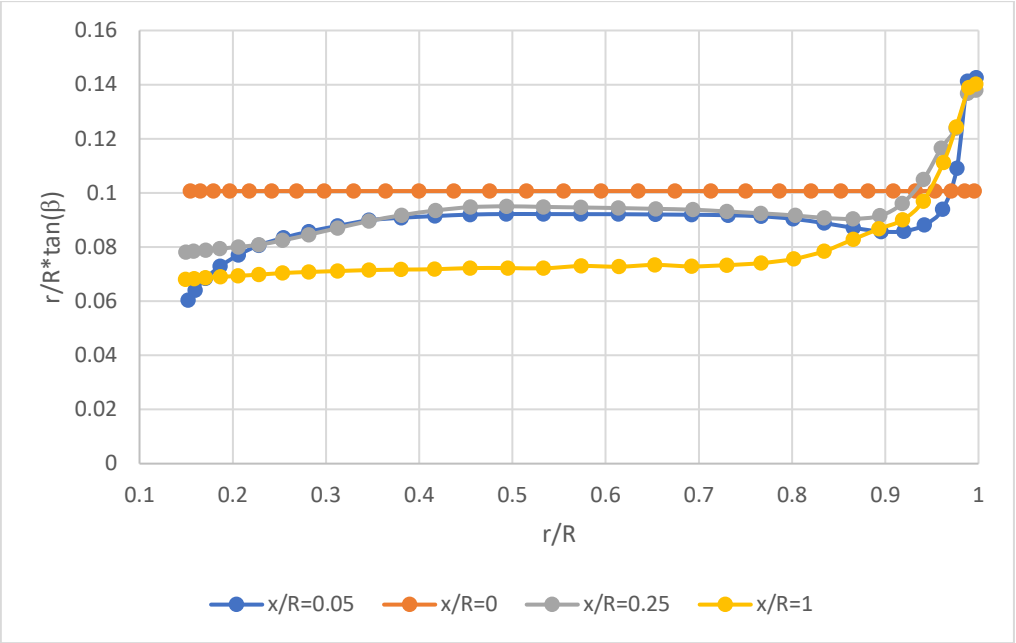

Figure 32: Pitch for given radial coordinates – inviscid case.

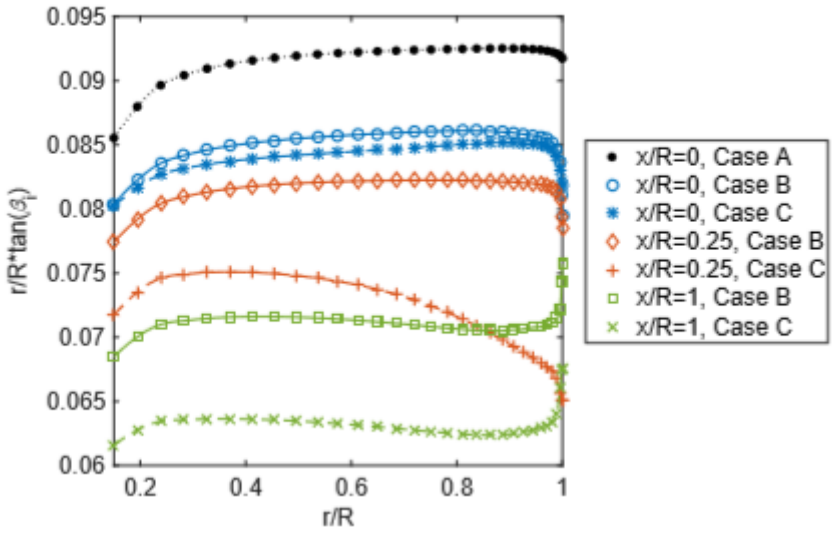

Figure 33: Pitch for given radial coordinates from (Sousa, 2018).

It is interesting to show not only the radial pitch distribution at different axial sections but also how the pitch at a given radial coordinate evolves going downstream. This is represented in Figure 34. Although some initial fluctuations from the trailing edge to $^{x}/_{R} = 0.8$ it is possible to conclude that the wake tries to keep a constant value of the pitch for each radial position, this makes total sense because we are moving downstream.

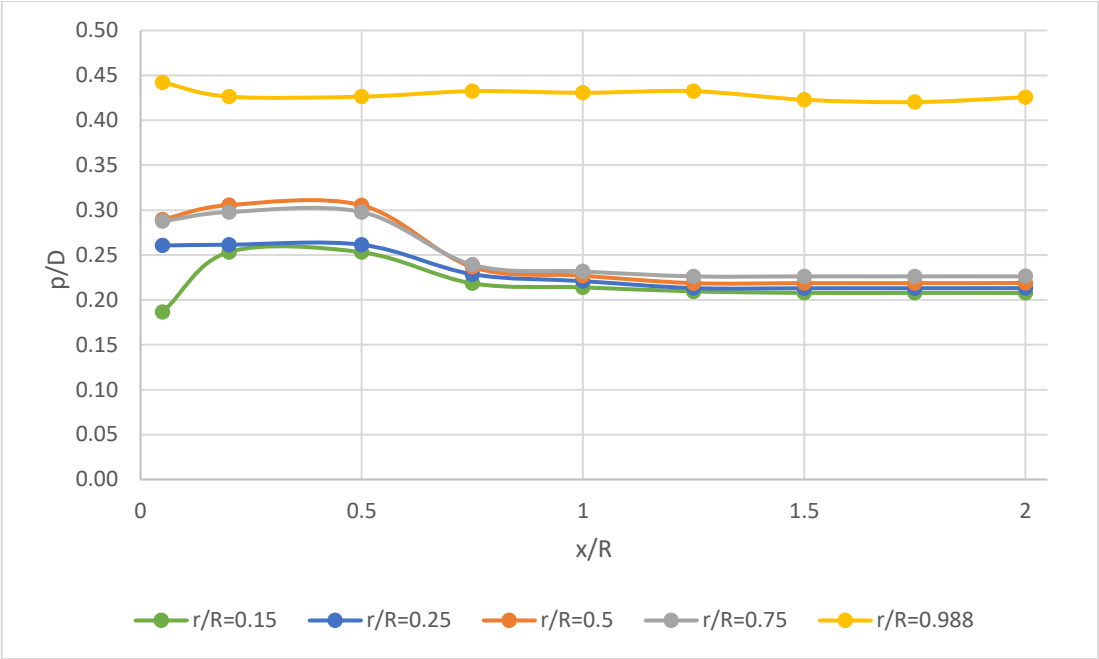

Figure 34: Pitch along the downstream direction – inviscid case.

The pitch above shown was obtained through the post processing code, however it is possible to compute the pitch far downstream from the induced velocities at the lifting line, based on the assumption mentioned in Optimization. In Figure 35 the pitch of the first design perfectly helicoidal wake is shown. At the lifting line it is constant as the optimization is classical while the pitch far downstream shows slightly higher value close to the root but after 20% of the blade length it is constant. The same trend can be observed in Figure 36 where the pitch at the lifting line and the pitch far downstream are shown for the third design iteration, where the wake is aligned with the local velocity. Again, it is possible to see that far downstream the pitch tries to be constant and the values are higher than the ones found with the first design.

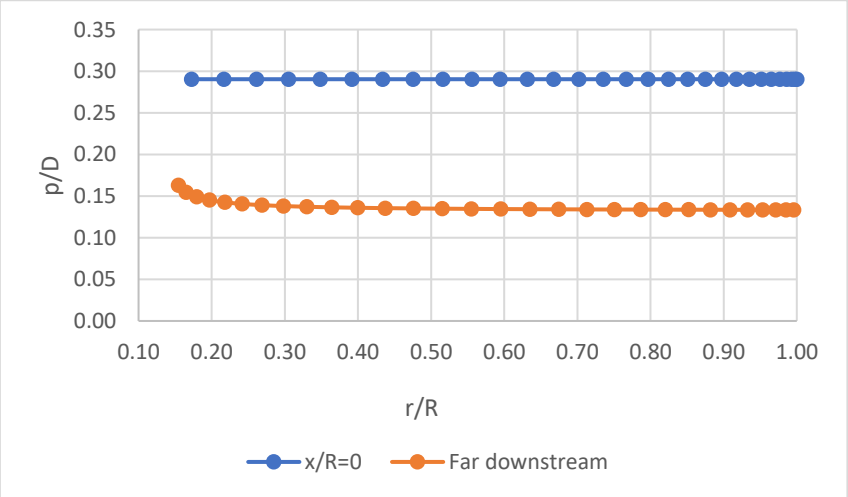

Figure 35: Pitch at the lifting line and far downstream based on the incuced velocities obtained at the lifting line – first design iteration - inviscid case.

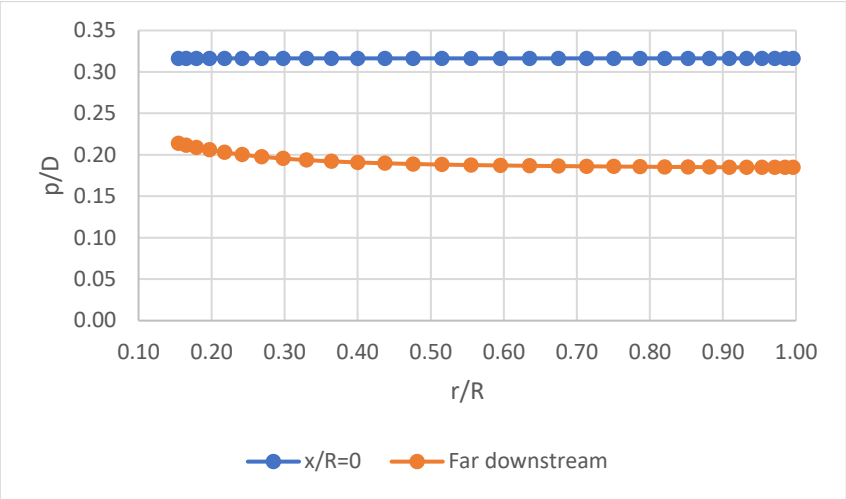

Figure 36: Pitch at the lifting line and far downstream based on the incuced velocities obtained at the lifting line – third design iteration - inviscid case.

The discussion of the results for the inviscid case finally ends showing the pressure distribution expressed in form of pressure coefficient (defined as $C_p = \frac{p-p_\infty}{\frac{1}{2}\rho {V_\infty}^2}$) at 3 different radial sections (Figure 37). The pressure varies in the chordwise direction as shown, the regions of lower and upper pression are easily recognizable and the shape of the graphs obtained is fully coherent with the ones coming from the work of (Hogan, 2010). The shape of the graphs does not change according to the blade radial section. Since the lift coefficient of 0.94 is constant along the whole blade, also the pressure coefficient is expected to have the same value of pressure regardless of the radial section analysed, therefore the differences between the values are due to the fact that aligning the wake also the lift coefficient distribution slightly changes.

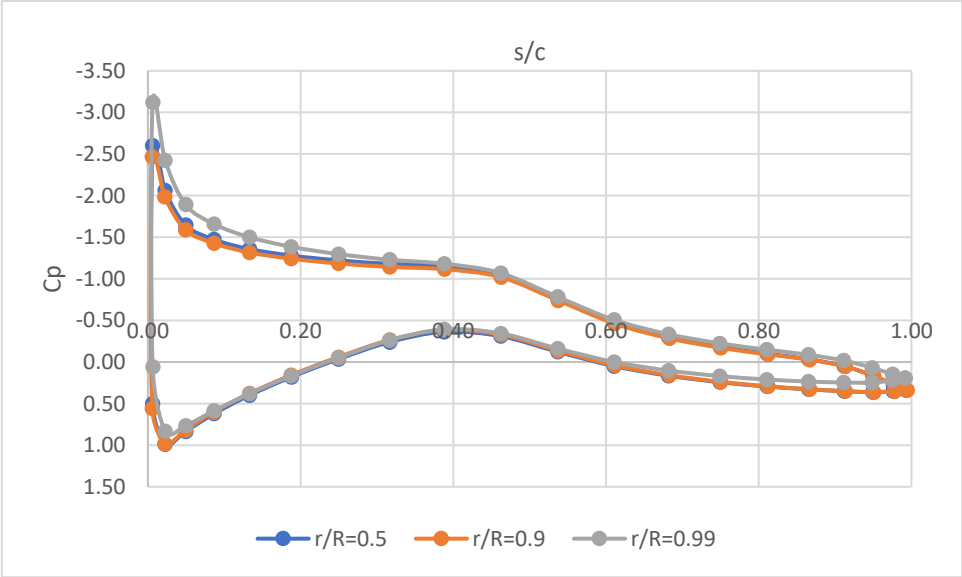

Figure 37: Pressure distributions at three radial sections – inviscid case.

4.4 Viscous results ($\varepsilon = 0.011$)

Before starting the discussion of the results obtained with the viscous assumption ($\varepsilon = 0.011$) it has to be said that many of the conclusions in terms of distributions are very similar to the ones presented in the Inviscid results and whenever this happens the author will summarize them quickly avoiding long repetitions.

The circulation distributions (Figure 38) of the second and third design are very similar, as it happens in the inviscid situation. It falls drastically down to zero after 80% of the blade length and the classical optimization is used.

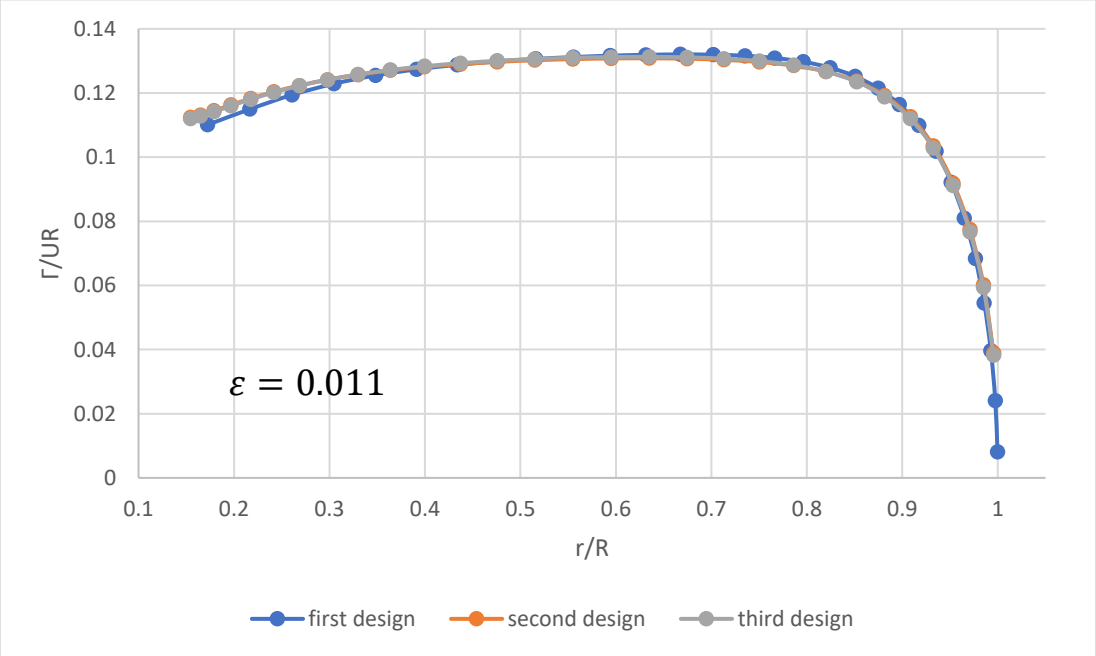

Figure 38: Circulation distribution – viscous case.

From the circulation distribution the design is done choosing the lift coefficient and the dimensionless pitch and chord distributions are obtained.

The second and third design graphs of blade pitch (Figure 39) and chord (Figure 40) show high similarity, as it happens in the inviscid case and the explanation of the trends is exactly the same. The differences in the values from the second to the third design are again below 2%.

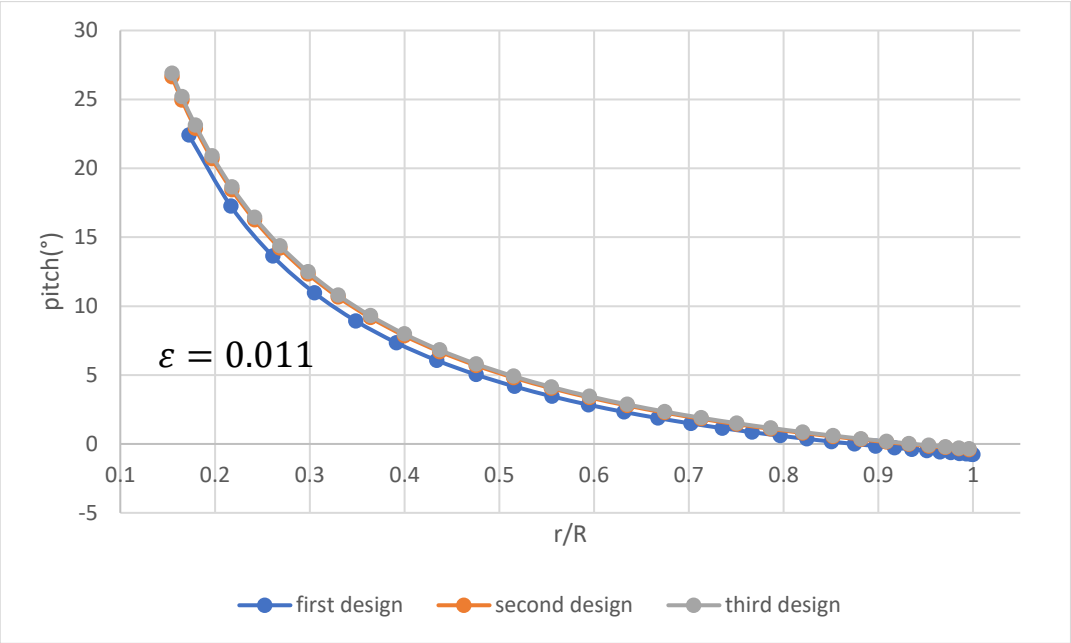

Figure 39: Blade pitch – viscous case.

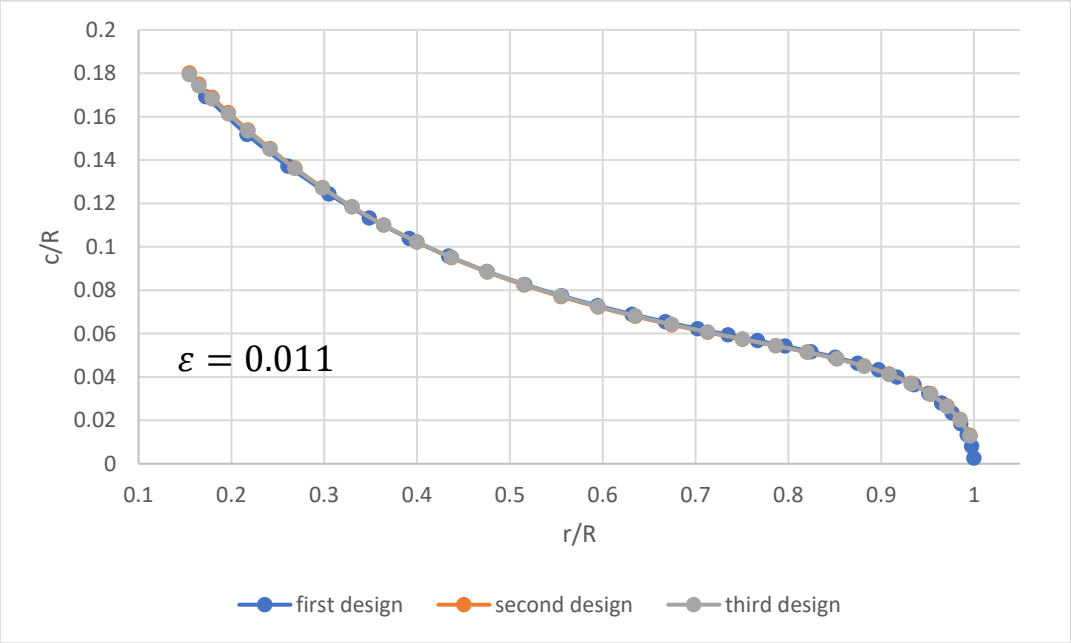

Figure 40: Chord – viscous case.

In the same way as done for the inviscid case procedure, the power coefficient is optimized in the first design and the corresponding thrust coefficient is used from that moment on when the lifting line design occurs. The panel code analysing the turbine gives as output the thrust and power coefficients that are not really interesting for us since the panel method calculation works in such a way that is not able to take into account the viscous effects. In order to correct those coefficients the drag effects must be taken into account and a

post processing code in which the distribution of drag and lift is provided as input is used: the thrust coefficient do not really change but the power coefficient does and it gets lower, approaching the one found with lifting line optimization. In fact, in the second cycle the power coefficient is 0.513 and the one found through viscous corrections is 0.529. Again, the convergence in terms of power coefficient is achieved: when the third lifting line optimization happens the power coefficient is 0.519, value very close to the second design power coefficient (0.513). All the values of thrust and power coefficients are reported in Table 5. The effect of aligning the wake lies on the increase of the power coefficient of around 5% from the first design (0.483) in which the wake is not aligned to the second design (0.513) where the wake is aligned with the airflow local velocity.

Lifting line code	**PROPAN code**	**PROPAN code (viscous effects)**
$C_T = 0.795$ $C_P = 0.483$	$C_T = 0.847$ $C_P = 0.575$	$C_T = 0.852$ $C_P = 0.532$
$C_T = 0.795$ $C_P = 0.513$	$C_T = 0.815$ $C_P = 0.570$	$C_T = 0.819$ $C_P = 0.529$
$C_T = 0.795$ $C_P = 0.519$		

Table 5: Thrust and power coefficients – viscous case.

The comparison of the circulation distributions obtained with the panel method code and the ones obtained through the lifting line code highlight again that the major differences lies on the region between the hub radius and 40% of the blade radius (Figure 41). However, it is possible to see that the circulation obtained using PROPAN the second time overlap with the third design after 60% of the blade radius.

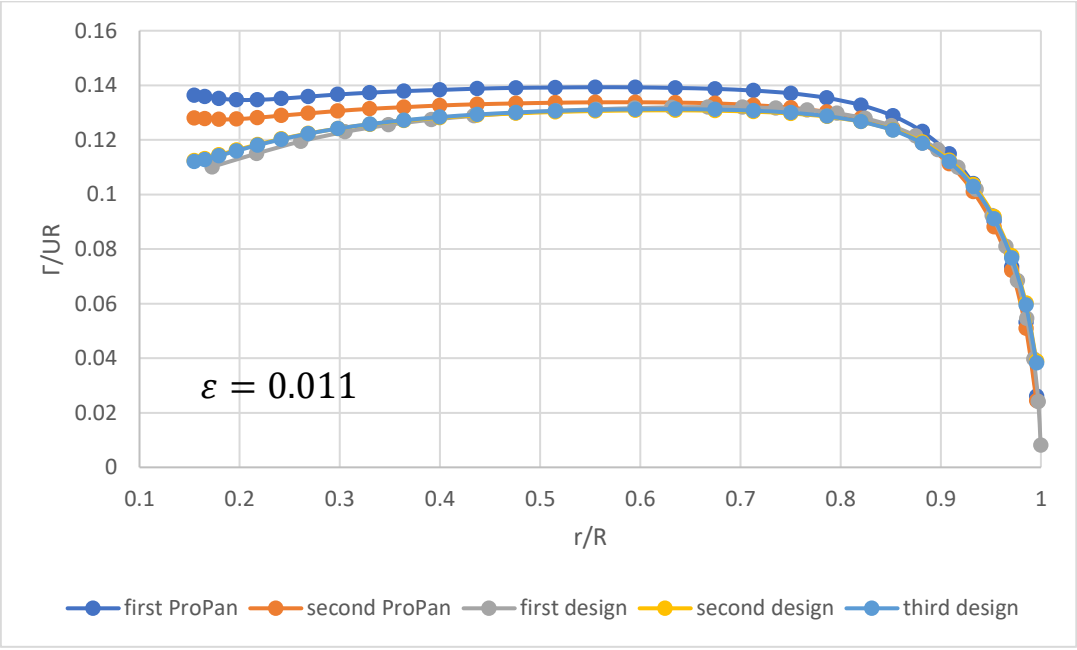

Figure 41: Comparison with the circulation distribution from PROPAN – viscous case.

The wakes are illustrated and again the first wake (Figure 42) is perfectly helicoidal, as it is not aligned and the pitch is uniform everywhere and equal to the lifting line one. The second and the third wakes (Figure 43 and Figure 44) folds in the downstream direction at any axial alignment section as expected. In this case it is not possible to compare the wake geometries with Sousa's results because he did not make any studies on the wake geometry with the viscous flow assumption.

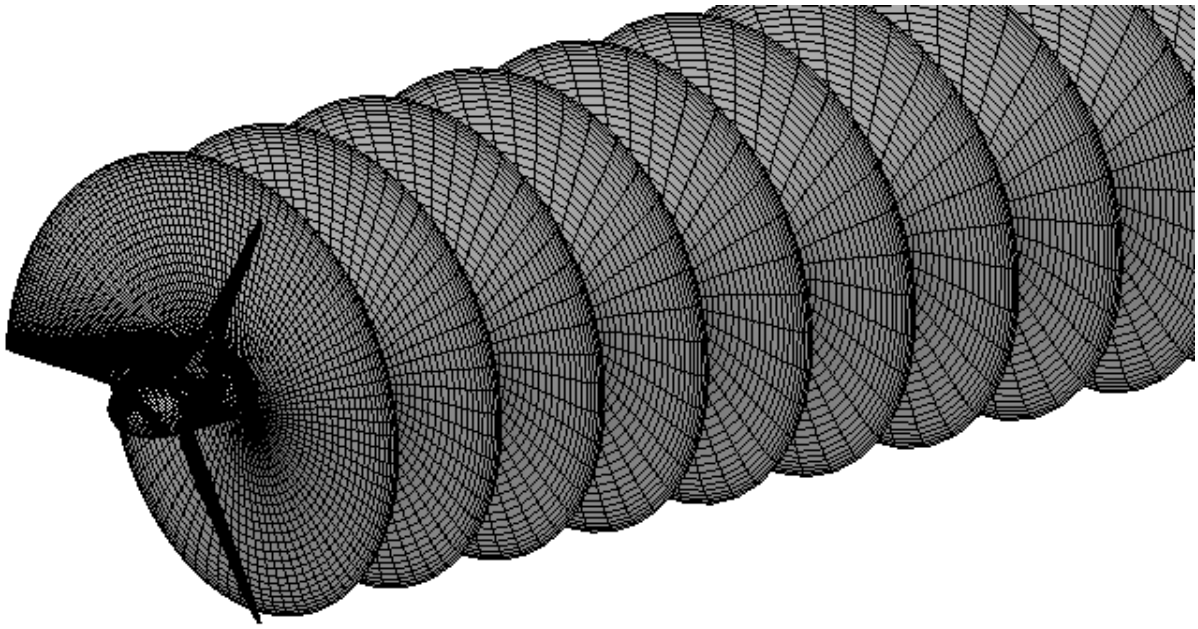

Figure 42: Helycoidal wake – viscous case.

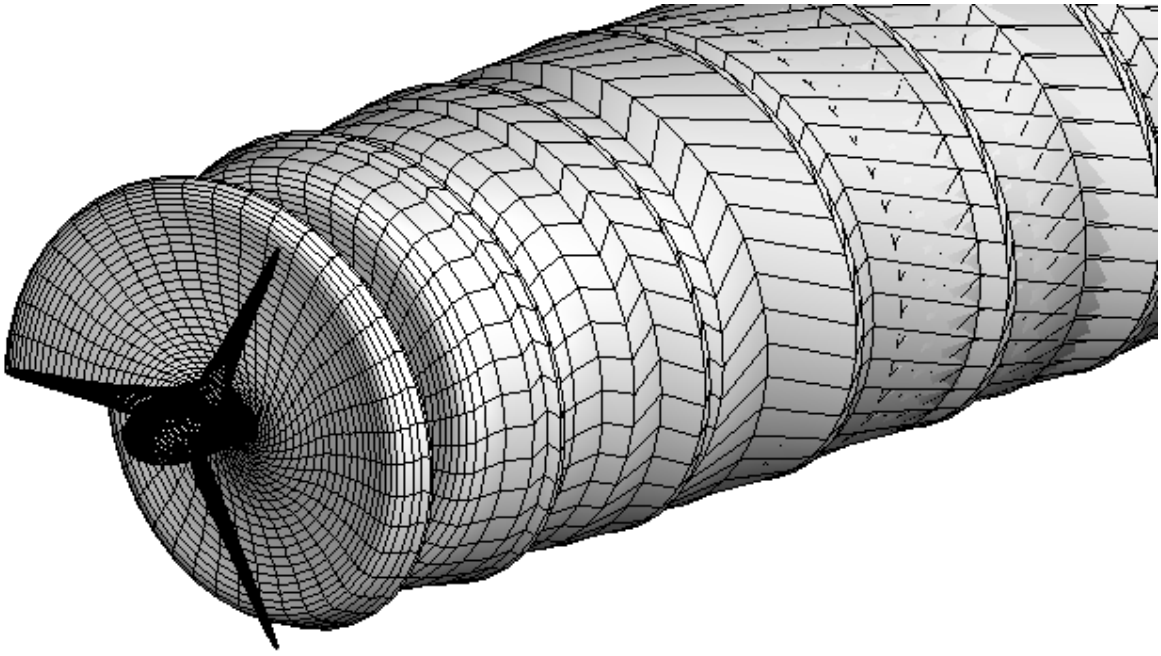

Figure 43: First aligned wake – viscous case.

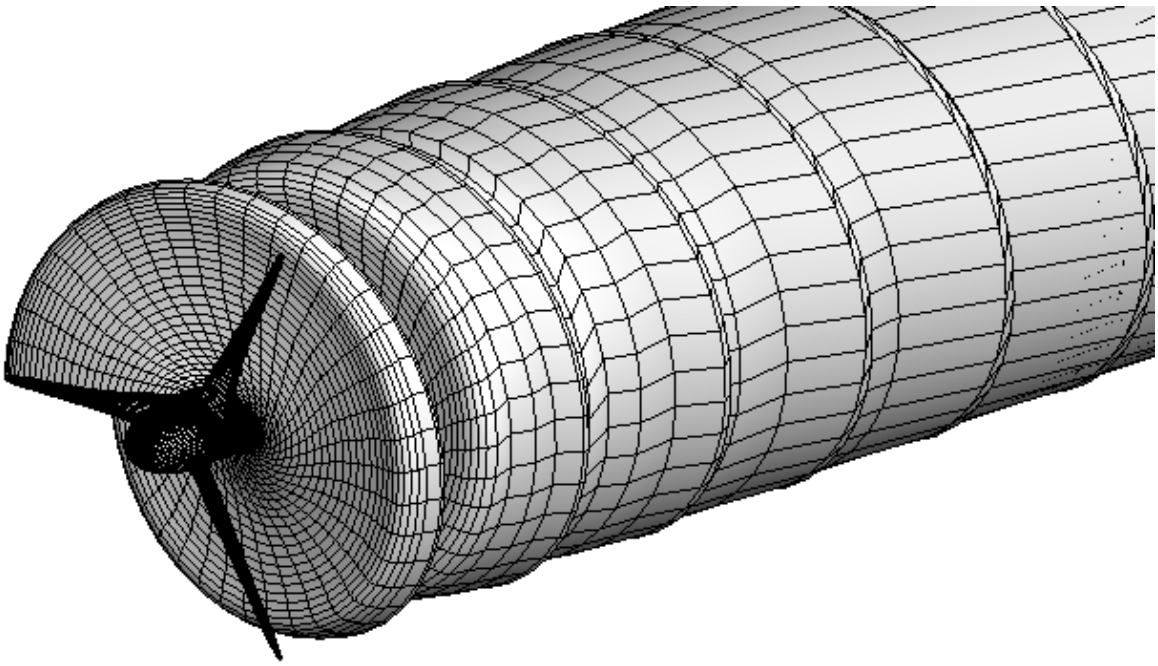

Figure 44: Second aligned wake – viscous case.

Looking at the pitch distributions at the axial sections r/R={0, 0.05, 0.25, 1} (Figure 45) it is possible to confirm the folding behaviour of the wake, in fact the pitch keeps its value constant until 80% of the blade length and then it increases. This does not happen at the lifting line where the pitch is constant because of the fact that the classical optimization is used.

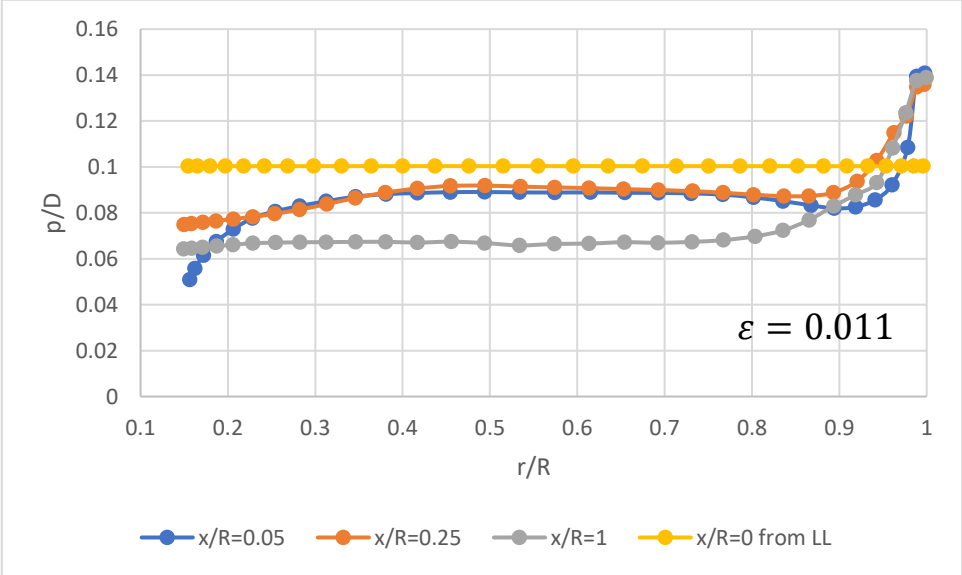

Figure 45: Pitch for given radial coordinates – viscous case.

The pitch along the downstream direction (Figure 46) shows that after an initial phase in which the values fluctuate, after the coordinate to $^{x}/_{R} = 0.7$ the pitch at each radial coordinate is almost constant, this happens because the transition wake is probably over and the pitch tries to behave constantly.

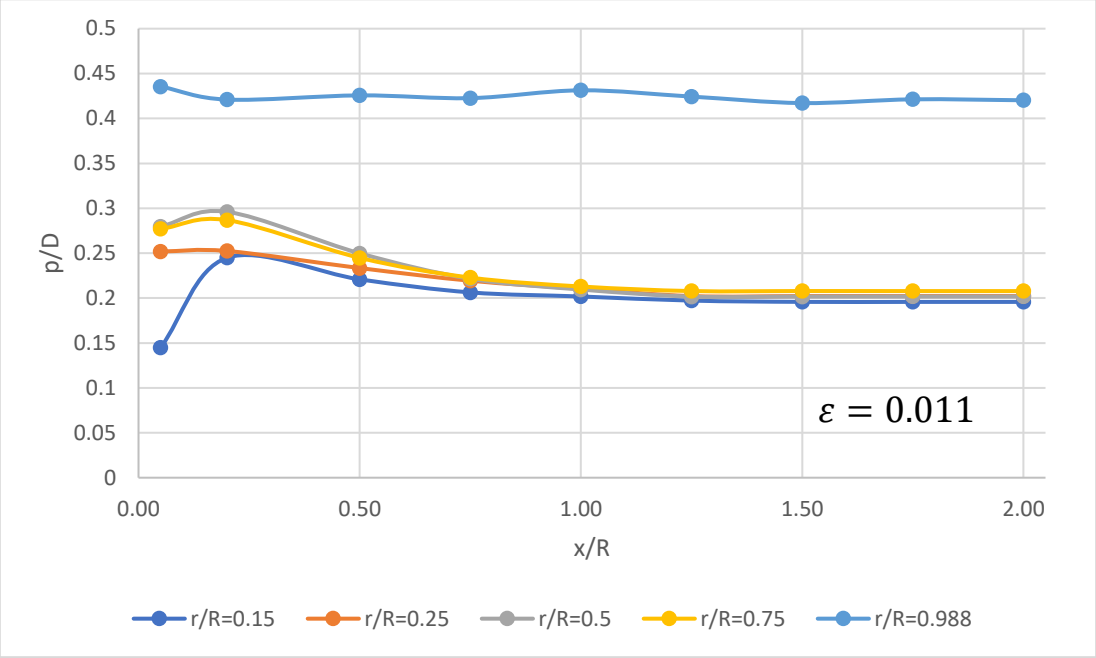

Figure 46: Pitch along the downstream direction – viscous case.

The pitch far downstream is calculated based on the induced velocities at the lifting line. In the case of the first design (Figure 47) the wake is perfectly helicoidal and the pitch obtained is constant after 30% of the blade length. The same trend can be observed in Figure 48 where the pitch at the lifting line and the pitch far downstream are shown for the third design, where the wake is aligned with the local velocity. Again, it is possible to see that far downstream the pitch tend to stabilize its value after 40% of the blade length and the values are higher than the ones found with the first design.

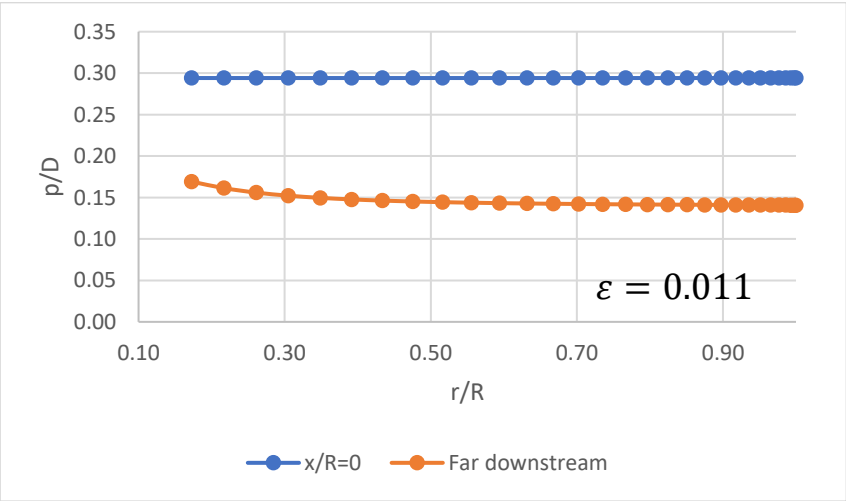

Figure 47: Pitch at the lifting line and far downstream based on the induced velocities obtained at the lifting line - first design iteration - viscous case.

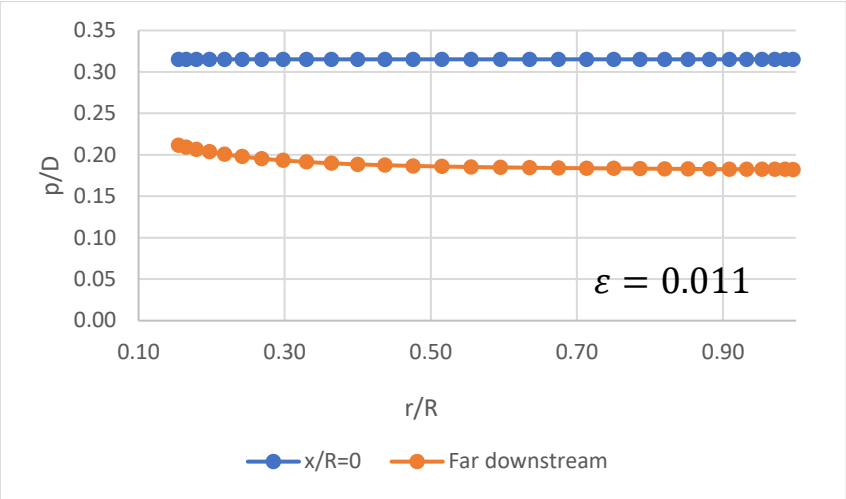

Figure 48: Pitch at the lifting line and far downstream based on the induced velocities obtained at the lifting line - third design iteration - viscous case.

The discussion of the results ends showing the pressure distribution at 3 different radial sections in Figure 49. The pressure varies in the chordwise direction as shown, the regions of lower and upper pression are easily recognizable and the shape of the graphs obtained is fully coherent with the ones coming from the literature (Hogan, 2010).

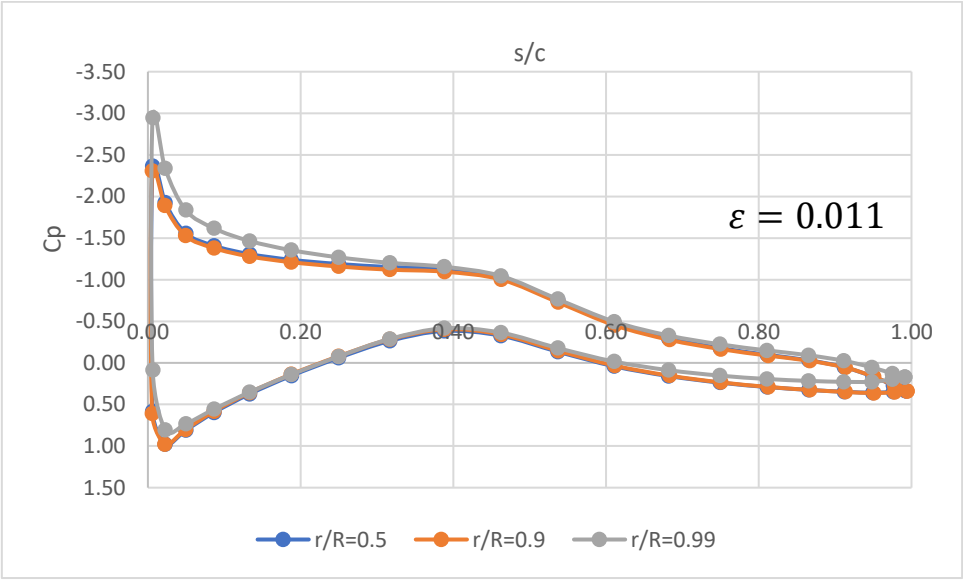

Figure 49: Pressure distributions at three radial sections – viscous case.

4.5 Comparison of inviscid and viscous design

In Table 6 the values of thrust and power coefficients corresponding to the final design of the rotor are reported. It is possible to conclude that the thrust and power coefficients are lower in the case of viscous flow, where the lift to drag coefficient is equal to 0.011. This was predictable looking at the Eq. 22 and it makes sense that the wind power extracted by the rotor is lower for the viscous case since the losses related to the viscosity of the flow are not neglected anymore.

Inviscid	**Viscous ($\varepsilon = 0.011$)**
$C_T = 0.804$	$C_T = 0.795$
$C_P = 0.562$	$C_P = 0.519$

Table 6: Thrust and power coefficients for the inviscid and viscous cases.

In terms of circulation distribution, the differences are very small, in fact in Figure 50 it is difficult to distinguish the inviscid from the viscous distribution. The highest difference along the radial coordinate is around 1%. A similar result was found by Chattot (2003) that showed viscous correction only causes a minor effect on the optimum geometry of the blade.

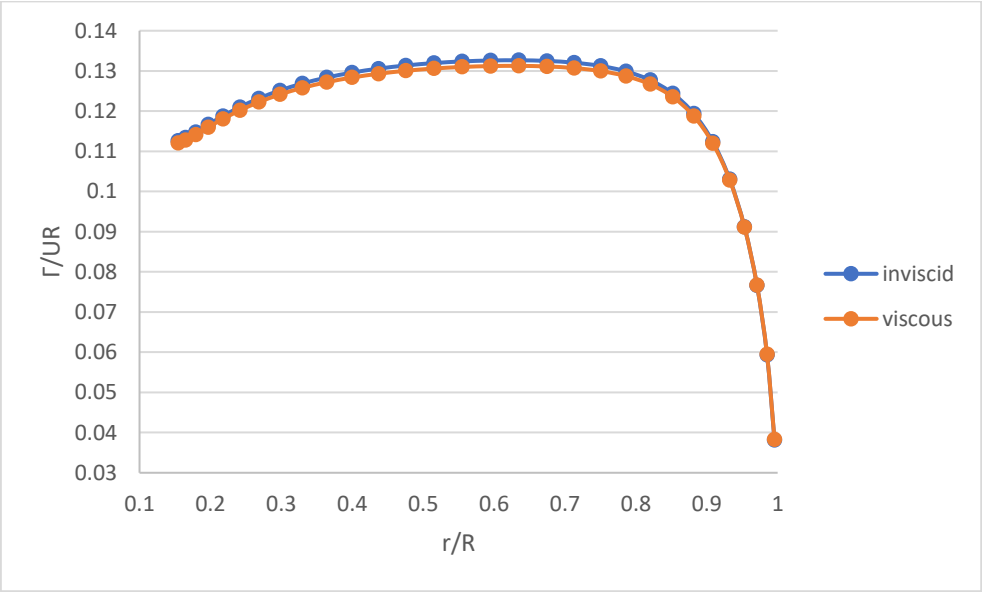

Figure 50: Comparisons of the circulation distributions between inviscid and viscous flow – third design iteration.

The aerodynamic pitch angle barely changes shifting from the inviscid flow assumption to the viscous one and this, together with the fact that the angle of attack is the same in the two cases, brings to a graph of the blade pitch (Figure 51) in which the two distributions exactly overlap.

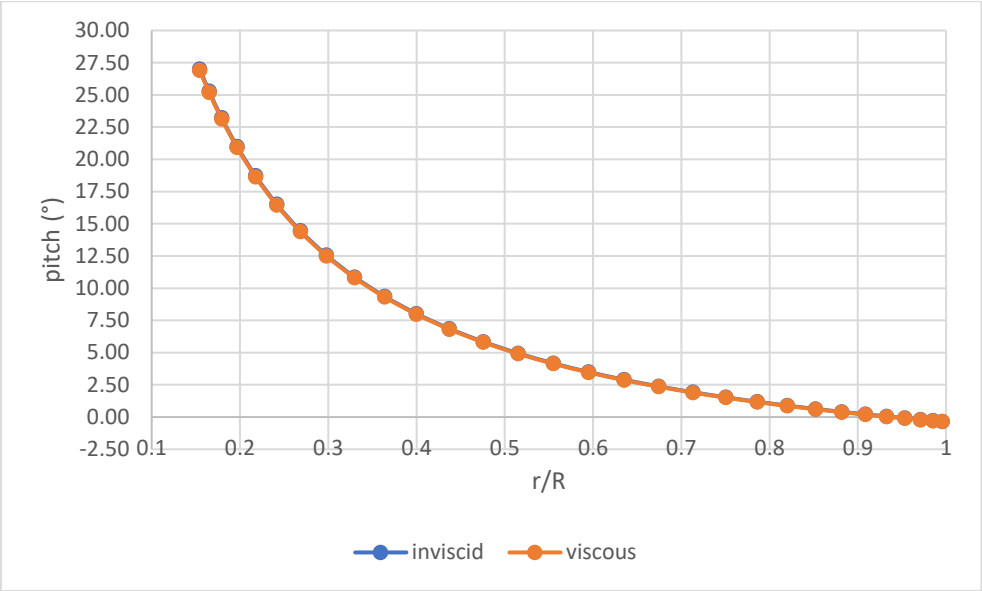

Figure 51: Comparison of the design blade pitch between inviscid and viscous flow.

The situation is slightly different in the case of the chord distribution (Figure 52), in fact the graphs are quite different, the variation of the two graphs is around 11% at every radial coordinate and the reason why this happen is related to the choice of the lift coefficient. The lift coefficient in the inviscid case is 0.94 while in the viscous one is 0.84 and this brings to a higher chord in the viscous case.

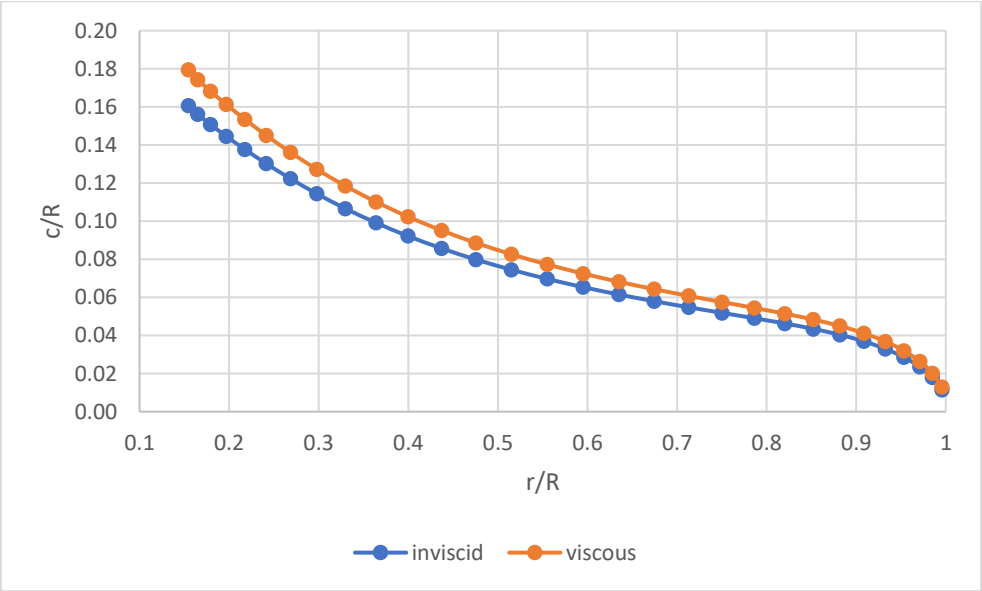

Figure 52: Comparison of the chord between the inviscid and viscous flow.

In Figure 53 it is possible to compare the wake pitch for both the inviscid and viscous flow at different selected axial sections. The trends of the dimensionless pitch is the same for every axial section but it is

possible to notice that the wake pitch in the case of inviscid flow is higher along the radius, from the root to the tip.

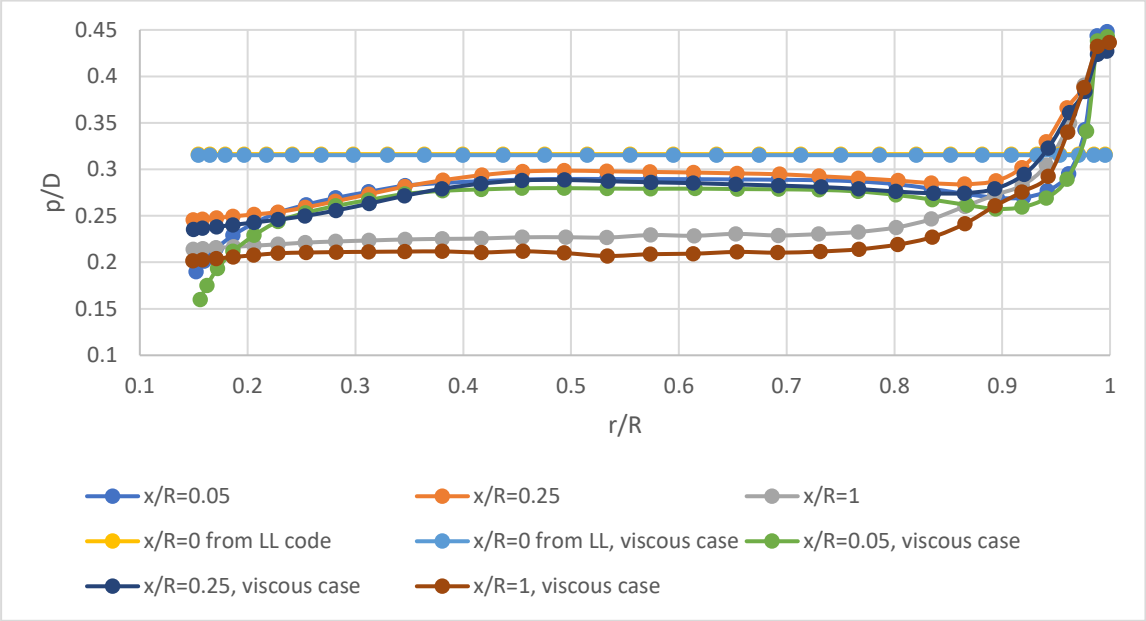

Figure 53: Comparison of the pitch distributions between the inviscid and viscous flow

It is possible to compare the pressure coefficient between the inviscid and viscous flow looking at Figure 54. The pressure coefficient distribution is very similar for each of the radial section chosen and the differences among those it is possible to be reconducted to the fact that the lift coefficient is different between the two cases and so the pressure distribution has to be.

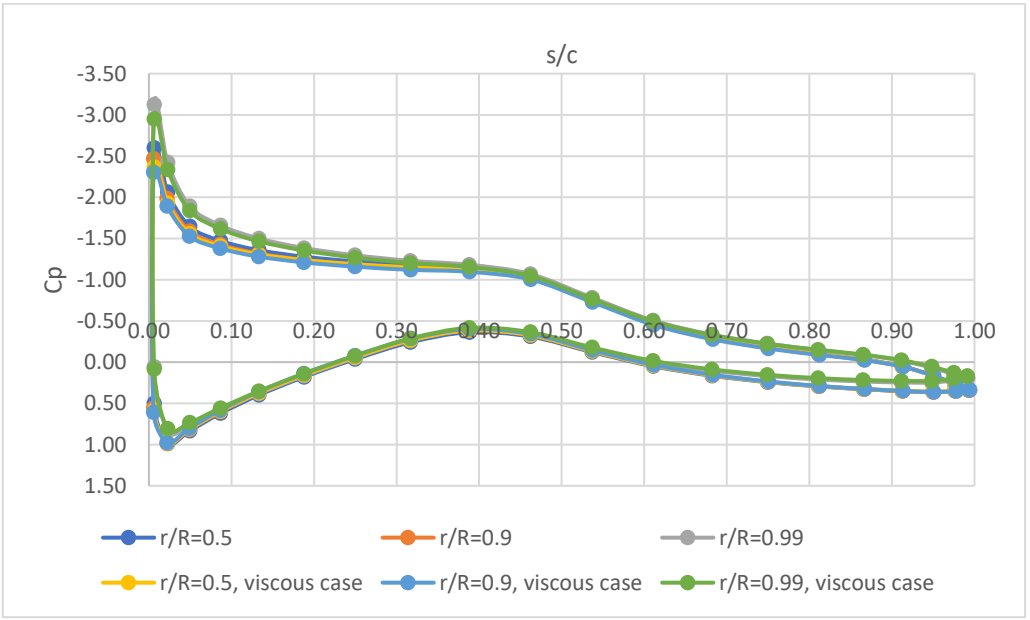

Figure 54: Comparison of the pressure coefficient between the inviscid and viscous flow

5 Conclusions

In this work the optimization procedure implemented in the work of Sousa (2018) is improved providing a new more accurate wake alignment method. In particular, the lifting line optimization procedure is combined with a code able to analyse the rotor through the boundary element method. The inviscid design of the blades is done starting from the optimum circulation distribution, choosing a lift coefficient and performing the blade design. The analysis of the rotor with the specified air inflow conditions is carried out and a wake geometry aligned with the local fluid velocity is obtained that it can be used as input in a second cycle for the lifting line optimization which is done based on the wake geometry obtained with the panel method code. The entire cycle may be repeated several times. It was noticed in fact, that after three lifting line optimizations the power coefficient increased showing convergence behaviour so it possible to stop the iteration lifting line code – panel method code. A convergence analysis on the in-house IST panel code PROPAN was conducted too, to show the effect of the choice of the alignment sections, the number of iterations and the number of panels per revolution of the wake.

Starting from the third circulation obtained and choosing a lift coefficient and the angle of attack, the design of the blades is done and the chord and pitch distributions obtained are in good agreement with the literature. It was shown that using the combination of lifting line and panel method a physically acceptable result was obtained. Using the lifting Line code for the wake alignment (Sousa, 2018) the pitch decreased toward the tip close to the rotor and at the lifting line (behaviour typical for a propeller). With the wake alignment procedure used in this study, the pitch distribution has the correct trend very close to the rotor plane $\left({}^{x}/_{R} = 0.05\right)$. Naturally, in all the other alignment sections downstream the behaviour of the pitch distribution is the right one, with the wake folding in the downstream direction.

The downstream behaviour of the wake show that after a transition wake region the pitch tends to stabilize. Far downstream a constant pitch distribution is obtained except towards the tip, the estimation is based on the induced velocities at the lifting line.

The viscous effects were investigated doing all the procedure above explained setting a drag to lift coefficient equal to 0.011. Again, the wake geometry obtained is physically acceptable but when it comes to compare the design with the inviscid one the only remarkable difference lies on the chord distribution, and this comes from the choice of the lift coefficient that in this case must be inevitably lower, due to the viscous effects that are playing a fundamental role.

In terms of future work there are many suggestions and improvements that could be done starting from the model shown. First of all, we were not able to use the Lagrange multiplier optimization in the lifting line and this would have set less constraints to the optimization problem. More efforts have to be put on the understanding of the weird wake geometries obtained through the panel method code using specific combinations of alignment sections and without removing some of the radial strips, they probably come from changing the blade pitch from negative values to slighty positive ones when using those values as input

in the Propanel code. Also parametric studies would show the effects of different tip speed ratios and drag to lift coefficients in terms of thrust and power coefficient and wake geometry too. It would be interesting to see if going ahead with the iterations lifting line code – panel method code the power coefficient would continuously converge and based on that the design would be done starting from the corresponding circulation distribution. Moreover, the design of the blade could be done in such a more realistic way in which the chord at the tip does not go to zero and the computation of the radial induced velocities could bring to the expansion of the wake. Finally, different choices of the lift coefficient and angle of attacks could show how the design of the blades would change.

References

Abbott, H. I. (1959). *Theory of Wing Sections*. (I. Dover Publications, Ed.). New York.

Adkins, C. N., & Liebeck, R. H. (1994). Design of optimum propellers. *Journal of Propulsion and Power*, *10*(5), 676–682. https://doi.org/10.2514/3.23779

Anderson, J. D. (2001). *Fundamental of aerodynamics*. McGraw-Hill, Boston.

Baltazar, J., & Falcão de Campos, J. A. C. (2009). Unsteady Analysis of a Horizontal Axis Marine Current Turbine in Yawed Inflow Conditions With a Panel Method. *First International Symposium on Marine Propulsors*, (June), 9.

Baltazar, J., & Falcão de Campos, J. A. C. (2011). Hydrodynamic Analysis of a Horizontal Axis Marine Current Turbine With a Boundary Element Method. *Journal of Offshore Mechanics and Arctic Engineering*, *133*(4), 041304. https://doi.org/10.1115/1.4003387

Baltazar, J., Falcão de Campos, J. A. C., & Bosschers, J. (2012). Open-Water Thrust and Torque Predictions of a Ducted Propeller System with a Panel Method. *International Journal of Rotating Machinery*, *2012*, 1–11. https://doi.org/10.1155/2012/474785

Baltazar, J., Machado, J., & Falcão de Campos, J. A. C. (2011). Hydrodynamic Design and Analysis of Horizontal Axis Marine Current Turbines With Lifting Line and Panel Methods (pp. 453–465). ASMEDC. Retrieved from https://asmedigitalcollection.asme.org/OMAE/proceedings/OMAE2011/44373/453/350993

Betz. (1919). Schraubenpropeller mit geringstem Energieverlust. Nachrichten von der Gesellschaft der Wissenschaften zu Gottingen, Mathematisch-Physikalische Klasse.

BP. (2018). *Statistical Review of World Energy*.

Caldeira, J. M. R. (2014). *Análise de um Modelo de Perda para o Cálculo Aerodinâmico da Turbina Eólica de Eixo Horizontal NREL / NWTC com o Método da Linha Sustentadora - MSc Thesis in Mechanical Engineering*. Instituto Superior Tecnico.

Chattot, J.-J. (2003). Optimization of Wind Turbines Using Helicoidal Vortex Model. *Journal of Solar Energy Engineering*, *125*(4), 418. https://doi.org/10.1115/1.1621675

Duarte, R. S., & Falcão de Campos, J. A. C. (1997). Numerical model of propeller vortex wakes for calculation of induced velocities, (1989).

EIA. (2017). EIA projects 28% increase in world energy use by 2040 - Today in Energy. Retrieved June 24, 2019, from https://www.eia.gov/todayinenergy/detail.php?id=32912

Erickson, L. (1990). *NASA Technical Paper Panel Methods-An Introduction*. Moffett Field, California.

Falcão de Campos, J. A. C. (2007). Hydrodynamic Power Optimization of a Horizontal Axis Marine Current Turbine with Lifting Line Theory. In *Proceedings of the Seventeenth (2017) International Offshore and Polar Engineering Conference* (pp. 307–313). Lisbon, Portugal.

Gallard. (2014). Aircraft Shape Optimization for Mission Performance. https://doi.org/10.13140/RG.2.2.15712.89607

Goldstein. (1929). On the Vortex Theory of the Screw Propeller. *Journal of the Aeronautical Sciences*, *5*(1), 1–7. https://doi.org/10.2514/8.496

Hogan, F. (2010). *Análise do Desempenho Aerodinâmico da turbina Eólica NREL com um Método de Elementos de Fronteira - MSc Thesis in Mechanical Engineering*. Instituto Superior Tecnico.

Kawada, S. (1933). On the induced velocities and characteristics of a propeller. *Journal of the Faculty of Engineering*.

Kerwin, J. E. (2001). *Lecture Notes Hydrofoils and Propellers*. *Lecture Note*. Cambridge.

Kerwin, J. E., Member, A., Kinnas, S. A., & Le, J. (1987). A Surface Panel Method for the Hydrodynamic Analysis of Ducted Propellers. New York: The society of naval architects and marine engineers.

Lanchester, F. W. (1907). *Aerodynamics*. Archibald Constable & Co. LTD.

Lerbs, H. W. (1952). Moderately Loaded Propellers with a Finite Number of Blades and an Arbitrary Distribution of Circulation. *Transactions of the Society of Naval Architects and Marine Engineer*, *60*(1952), 73–123.

Lighthill, J., & Berger, S. A. (2008). An Informal Introduction to Theoretical Fluid Mechanics. *Physics Today*, *41*(6), 84–86. https://doi.org/10.1063/1.2811466

Machado, J. L. (2010). *Projecto hidrodinâmico de turbinas de corrente marítima de eixo horizontal com o modelo da linha sustentadora - MSc Thesis in Mechanical Engineering*. Instituto Superior Tecnico.

Maekawa, H. (1986). Optimum design method of Horizontal-axis wind turbine blades based on lifting-line theory. *Bulletin of JSME*, (43), 2091. Retrieved from http://www.mendeley.com/research/geology-volcanic-history-eruptive-style-yakedake-volcano-group-central-japan/

Melo, D. B. (2016). *Analysis of Horizontal Axis Wind Turbines with Lifting Line Theory - MSc Thesis in Mechanical Engineering*. Insituto Superior Tecnico.

Morino, L., & Kuo, C. . (1974). Subsonic Potential Aerodynamics for Complex Configurations : A General Theory. *AIAA Journal*, *12*(2), 191–197. https://doi.org/10.2514/3.49191

Nelson, B., & Kouh, J.-S. (2017). The Aerodynamic Analysis of a Rotating Wind Turbine by Viscous-Coupled 3D Panel Method. *Applied Sciences*, *7*(6), 551. https://doi.org/10.3390/app7060551

Prandtl, L. (1918). *Tragflügeltheorie*. Königliche Gesellscahft der Wissenschaften zu Göttingen.

Ribeiro, M. H. D., & Falcão de Campos, J. A. C. (2003). Optimization of propeller blade distribution of circulation with the lifting line model including section drag effects. In *VII Congresso de Mecânica Aplicada e Computacional*. Evora, Portugal.

Salvatore, F., Sarichloo, Z., & Calcagni, D. (2018). Marine Turbine Hydrodynamics by a Boundary Element Method with Viscous Flow Correction. *Journal of Marine Science and Engineering*, *6*(2), 53. https://doi.org/10.3390/jmse6020053

Sousa, G. (2018). *Aerodynamic Optimization of Horizontal Axis Wind Turbines Using the Lifting Line Theory Gonçalo dos Santos Sousa - MSc Thesis in Mechanical Engineering*. Instituto Superior Tecnico.

Sun&Wind Energy. (2017). Total offshore wind capacity in Europe stands at 12.631 MW. Retrieved June 24, 2019, from http://www.sunwindenergy.com/offshore-wind-energy/total-offshore-wind-capacity-europe-stands-12631-mw

UNFCCC. (2018). The Paris Agreement. Retrieved June 24, 2019, from https://unfccc.int/process-and-meetings/the-paris-agreement/the-paris-agreement

Yahyaoui, I. (2018). *Advances in renewable energies and power technologies. Volume 1, Solar and wind energies*. Elsevier Science.